Title: Cooperative epithelial phagocytosis enables error correction in the early embryo

Author list: Esteban Hoijman[1,*], Hanna-Maria Häkkinen[1], Queralt Tolosa-Ramon[1], Senda Jiménez- Delgado, Chris Wyatt[1], Marta Miret-Cuesta[1], Manuel Irimia[1,2,3], Andrew Callan-Jones[4], Stefan Wieser[5,*], Verena Ruprecht[1,2,*]

Affiliations:
[1] Centre for Genomic Regulation (CRG), The Barcelona Institute of Science and Technology, 08003 Barcelona, Spain
[2] Universitat Pompeu Fabra (UPF), Barcelona, Spain
[3] ICREA, Barcelona, Spain
[4] Laboratoire Matière et Systèmes Complexes, CNRS/Université Paris-Diderot, UMR 7057, 75205
Paris Cedex 13, France
[5] ICFO – Institut de Ciencies Fotoniques, The Barcelona Institute of Science and Technology,08860 Castelldefels, Spain

* Correspondence to esteban.hoijman@crg.eu, Stefan.Wieser@icfo.eu, verena.ruprecht@crg.eu

Summary
Errors in early embryogenesis are a cause of sporadic cell death and developmental failure1,2. Phagocytic activity has a central role in scavenging apoptotic cells in differentiated tissues3,4,5,6. However, how apoptotic cells are cleared in the blastula embryo in the absence of specialized immune cells remains unknown. Here we show that the surface epithelium of zebrafish and mouse embryos, which is the first tissue formed during vertebrate development, performs efficient phagocytic clearance of apoptotic cells through phosphatidylserine-mediated target recognition. Quantitative four-dimensional in vivo imaging analyses reveal a collective epithelial clearance mechanism that is based on mechanical cooperation by two types of Rac1-dependent basal epithelial protrusions. The first type of protrusion, phagocytic cups, mediates apoptotic target uptake. The second, a previously undescribed type of fast and extended actin-based protrusion that we call ‘epithelial arms’, promotes the rapid dispersal of apoptotic targets through Arp2/3-dependent mechanical pushing. On the basis of experimental data and modelling, we show that mechanical load-sharing enables the long-range cooperative uptake of apoptotic cells by multiple epithelial cells. This optimizes the efficiency of tissue clearance by extending the limited spatial exploration range and local uptake capacity of non-motile epithelial cells. Our findings show that epithelial tissue clearance facilitates error correction that is relevant to the developmental robustness and survival of the embryo, revealing the presence of an innate immune function in the earliest stages of embryonic development.

Main text
Early embryogenesis is prone to cellular errors like mitotic defects induced by cell intrinsic or extrinsic stress factors[1,2]. This leads to sporadic cell death of progenitor stem cells[3-6], assumed to be a major cause of early developmental failures in human pre-implantation development[7,8]. Stochastic cell death is expected to occur at random locations, vary in cell number and differ from developmentally programmed cell death occurring at later stages in vertebrate embryogenesis, which has predefined spatiotemporal dynamics and specific functions in morphogenetic processes[9]. Detection and removal of cell corpses requires specific clearance mechanisms as mediated by professional phagocytic cells in adult tissues[10]. Whether such active mechanisms for efficient apoptotic tissue clearance exist in early blastula and gastrula

stages of vertebrate development is still not understood. At early blastula stage, the vertebrate embryo consists of an undifferentiated inner cell mass covered by a squamous surface epithelium, termed epithelial enveloping layer (EVL) in zebrafish and trophoblast in mouse. This epithelial layer represents the first tissue formed during vertebrate development and is considered to provide mechanical protection and physical barrier function in the early embryo[11,12]. To identify how apoptotic events are managed during early embryo development, we performed quantitative 4D in vivo imaging to visualize the spatio-temporal dynamics of single apoptotic cells. Live imaging of spontaneous progenitor cell death in the zebrafish blastula showed typical hallmarks of apoptosis such as cellular shape changes (Fig. 1a, Supplementary Video 1), cell and nuclear fragmentation (Fig. 1a, Extended Data Fig. 1a,c, Supplementary Video 1), PS exposure (Extended Data Fig. 1a, Supplementary Video 1), and Caspase-3 activation (Extended Data Fig. 1b, Supplementary Video 1). We observed that apoptotic events were frequently associated with errors in cell division such as aberrations in chromosome segregation (Extended Data Fig. 1c, Supplementary Video 2 and 11). Strikingly, spatio-temporal tracking of apoptotic progenitor cells dying in the embryo interior revealed their accumulation inside the EVL (Fig. 1a, Supplementary Video 1), suggesting that embryonic epithelial cells have a specific uptake capability. To probe the ability of early embryos to cope with an increased amount of cell death, we next challenged zebrafish blastula embryos by mosaic overexpression of the pro-apoptotic protein Bax[13] (Bax^{+} cells) to induce apoptotic cell death ectopically, as confirmed by *in vivo* analysis of PS exposure (Extended Data Fig. 1d) and Caspase-3 activation (Extended Data Fig. 1e-e', Supplementary Video 3). Remarkably, embryo survival was not significantly affected in conditions showing abundant cell death in the embryo (such as 2 pg of bax mRNA, Fig. 1b,c), suggesting the existence of an efficient failure compensation program in the embryo. Comparable to endogenous apoptotic events, extensive epithelial uptake was observed for Bax^{+} cells (Fig. 1c, Supplementary Video 3), revealing a high clearance capacity of the embryonic epithelium (Fig. 1c,d), with average removal rates of 68 +/- 3 apoptotic particles within 2 hours in the field of view. In contrast, only a very low uptake rate by progenitor cells was identified (Fig. 1e), showing that apoptotic cell clearance is epithelium-specific. Similar to Bax overexpression, tissue clearance by the EVL was observed by mosaic activation of the apoptotic effector molecule $Caspase\text{-}8^{ERT2}$ (Extended Data Fig. 1f, Supplementary Video 4). We further mimicked different intrinsic and extrinsic stress factors triggering cell death that can occur during early development: 1) impairing of DNA replication by mosaic overexpression of a mutant form of Topoisomerase-II[14], 2) transplantation of UV-irradiated cells, and 3) triggering mitochondrial stress in the whole embryo by pharmacological treatment with Raptinal[15] (Extended Data Fig. 2a-c). Epithelial clearance of apoptotic cells was consistently observed in all these conditions across the epithelium, supporting that clearance does not depend on the induction of a specific apoptotic program and the whole epithelium is competent for target uptake (Extended Data Fig. 2d-f, Supplementary Video 4). In addition, clearance did not depend on the presence of a high number of apoptotic events, as transplantation of only few apoptotic cells (4 +/- 3 cells) was sufficient to elicit epithelial uptake (Extended Data Fig. 2g). Moreover, induction of programmed cell death in a single progenitor cell by two-photon illumination *in vivo* resulted in efficient epithelial uptake (Extended Data Fig. 2h, Supplementary Video 4), supporting a high sensitivity of the epithelium to detect and clear dying cells in the embryo. Together, these observations reveal a generic clearance function of the epithelium, establishing an error-correction mechanism present at blastula stages of embryonic development. Importantly, epithelial uptake operates across a broad range of apoptotic cell numbers, with efficient clearing of both single cells and massive regions of cell death.

apoptotic tissue clearance exist in early blastula and gastrula stages of vertebrate development is still not understood.

At early blastula stage, the vertebrate embryo consists of an undifferentiated inner cell mass covered by a squamous surface epithelium, termed epithelial enveloping layer (EVL) in zebrafish and trophoblast in mouse. This epithelial layer represents the first tissue formed during vertebrate development and is considered to provide mechanical protection and physical barrier function in the early embryo[11,12]. To identify how apoptotic events are managed during early embryo development, we performed quantitative 4D in vivo imaging to visualize the spatio-temporal dynamics of single apoptotic cells. Live imaging of spontaneous progenitor cell death in the zebrafish blastula showed typical hallmarks of apoptosis such as cellular shape changes (Fig. 1a, Supplementary Video 1), cell and nuclear fragmentation (Fig. 1a, Extended Data Fig. 1a,c, Supplementary Video 1), PS exposure (Extended Data Fig. 1a, Supplementary Video 1), and Caspase-3 activation (Extended Data Fig. 1b, Supplementary Video 1). We observed that apoptotic events were frequently associated with errors in cell division such as aberrations in chromosome segregation (Extended Data Fig. 1c, Supplementary Video 2 and 11). Strikingly, spatio-temporal tracking of apoptotic progenitor cells dying in the embryo interior revealed their accumulation inside the EVL (Fig. 1a, Supplementary Video 1), suggesting that embryonic epithelial cells have a specific uptake capability.

To probe the ability of early embryos to cope with an increased amount of cell death, we next challenged zebrafish blastula embryos by mosaic overexpression of the pro-apoptotic protein Bax[13] (Bax^+ cells) to induce apoptotic cell death ectopically, as confirmed by *in vivo* analysis of PS exposure (Extended Data Fig. 1d) and Caspase-3 activation (Extended Data Fig. 1e-e', Supplementary Video 3). Remarkably, embryo survival was not significantly affected in conditions showing abundant cell death in the embryo (such as 2 pg of bax mRNA, Fig. 1b,c), suggesting the existence of an efficient failure compensation program in the embryo. Comparable to endogenous apoptotic events, extensive epithelial uptake was observed for Bax^+ cells (Fig. 1c, Supplementary Video 3), revealing a high clearance capacity of the embryonic epithelium (Fig. 1c,d), with average removal rates of 68 +/- 3 apoptotic particles within 2 hours in the field of view. In contrast, only a very low uptake rate by progenitor cells was identified (Fig. 1e), showing that apoptotic cell clearance is epithelium-specific. Similar to Bax overexpression, tissue clearance by the EVL was observed by mosaic activation of the apoptotic effector molecule Caspase-8^{ERT2} (Extended Data Fig. 1f, Supplementary Video 4).

We further mimicked different intrinsic and extrinsic stress factors triggering cell death that can occur during early development: 1) impairing of DNA replication by mosaic overexpression of a mutant form of Topoisomerase-II[14], 2) transplantation of UV-irradiated cells, and 3) triggering mitochondrial stress in the whole embryo by pharmacological treatment with Raptinal[15] (Extended Data Fig. 2a-c). Epithelial clearance of apoptotic cells was consistently observed in all these conditions across the epithelium, supporting that clearance does not depend on the induction of a specific apoptotic program and the whole epithelium is competent for target uptake (Extended Data Fig. 2d-f, Supplementary Video 4). In addition, clearance did not depend on the presence of a high number of apoptotic events, as transplantation of only few apoptotic cells (4 +/- 3 cells) was sufficient to elicit epithelial uptake (Extended Data Fig. 2g). Moreover, induction of programmed cell death in a single progenitor cell by two-photon illumination *in vivo* resulted in efficient epithelial uptake (Extended Data Fig. 2h, Supplementary Video 4), supporting a high sensitivity of the epithelium to detect and clear dying cells in the embryo. Together, these observations reveal a generic clearance function of the epithelium, establishing an error-correction mechanism present at blastula stages of embryonic development. Importantly, epithelial uptake operates across a broad range of apoptotic cell numbers, with efficient clearing of both single cells and massive regions of cell death.

To obtain mechanistic insight into the apoptotic clearance process by epithelial cells, we visualized apoptotic uptake dynamics in individual epithelial cells expressing Lifeact-GFP (F-actin marker) *in vivo*. High-resolution imaging of Bax^{+} cells uptake events revealed the formation of characteristic phagocytic cups at the basal epithelial surface (facing the interior side of the embryo), representing dynamic actin-rich structures that progressively engulf and ingest apoptotic targets (Fig. 1f and Extended Data Fig. 3a, Supplementary Video 5). During ingestion, F-actin was depleted from the contact surface between the apoptotic and epithelial cell, forming a ring at the pseudopod front around the apoptotic target (Fig. 1f and Extended Data 3a-b, Supplementary Video 5). Cell shape analysis during the uptake process showed significant deformations of apoptotic targets, indicative of localized mechanical compressive forces exerted by phagocytic cups in the region of the actin ring (Fig. 1f and Extended Data Fig. 3a-d, Supplementary Video 5). Actin further accumulated in the final pseudopod closure site accompanied by local inward bending of the target, suggesting its pushing into the epithelial cell interior (Fig. 1f, Supplementary Video 5). Phagocytic cups were observed to be formed at the basal epithelial surface both from medial and lateral regions, with the latter extending dynamic membrane ruffles[16] (Extended Data Fig. 3e-f, Supplementary Video 5), which represent specific actin-rich lamellipodia-like protrusions[17]. We also observed that phagocytic protrusions can perform pruning of apoptotic cells, leading to apoptotic cell splitting and iterative apoptotic cell fragmentation underlying the wide range of uptaken particle sizes observed in epithelial cells (Extended Data Fig. 3g).

General upstream regulators of actin-based phagocytic cup formation have been identified, with the GTPase Rac1 mediating apoptotic phagocytosis in multiple physiological and pathological contexts[18-20]. Genetic interference using a dominant negative form of Rac1 (dnRac1) expressed in single epithelial cells blocked phagocytic uptake (Fig. 1g and Extended Data Fig. 4a). In addition, pharmacological interference with PI3K, a kinase regulating phagocytic cup dynamics[21], indicated that its activity is also required for embryonic epithelial phagocytosis (Extended Data Fig. 4b,c). These results establish that phagocytic target uptake by epithelial cells is mediated by a Rac1-PI3K-dependent signalling pathway.

Dynamic analysis of intracellular vesicles formed upon target engulfment showed that they represent functional phagosomes similar to the ones observed in professional phagocytes: 1) they present plasma membrane from both the epithelial phagocyte and the apoptotic cell (Extended Data Fig. 4d,e), 2) generate superoxide anions (Extended Data Fig. 4f), and 3) degrade the internal vesicle content, as visualized after apoptotic target ingestion by a decrease of Lifeact-GFP signal and the loss of plasma membrane localization of Lyn-TdTomato (Extended Data Fig. 4g-j). In agreement with a known role of integrins in phagocytosis[22], we further identified Itga5 as a marker of epithelial phagosomes (Extended Data Fig. 4k).

Altogether, these results indicate that the EVL performs active embryonic tissue clearance by phagocytic uptake of apoptotic cells employing similar mechanism than the ones described in professional phagocytes[10].

To identify how EVL cells recognize apoptotic cells before uptake, we analysed the relevance of PS exposure by apoptotic cells, which has been shown to mediate apoptotic cell uptake by professional phagocytes[23]. Injection of the PS-binding protein AnnexinV into the embryo at 4 hpf to decorate the surface of dead cells significantly impaired apoptotic cell clearance (Extended Data Fig. 5a,b). In addition, transplantation of surrogate apoptotic targets based on lipid vesicles confirmed that the presence of PS (PS^{+}) was required and sufficient for their recognition and epithelial phagocytosis *in vivo* (Fig. 1h and Extended Data Fig. 5c, Supplementary Video 6), with similar phagocytic cup formation dynamics (Extended Data Fig. 5d, Supplementary Video 6) as observed during apoptotic cell uptake (Fig. 1f). Consistently with a role of PS in target uptake, injection of a high number of PS negative (PS^{-}) surrogate targets caused abundant developmental failure, while adding PS to surrogate targets significantly increased embryo survival (Extended Data Fig. 5e), supporting that the presence of PS on the target surface promotes embryo survival. Notably,

performing a cross-species transplantation of UV-irradiated apoptotic human Jurkat T cells into zebrafish embryos further confirmed phagocytic uptake (Extended Data Fig. 5f,g), suggesting that conserved properties on the apoptotic target surface are sufficient for interspecies target recognition and uptake. Altogether, these results show that apoptotic cells are recognized by the EVL through PS-dependent mechanisms, mediating tissue clearance and restoration of embryo homeostasis.

To analyse the global gene expression profile involved in the phagocytic function of the surface embryonic epithelium, we performed RNA-Seq on EVL cells and progenitor stem cells of the blastula embryo. Genes that were upregulated in the EVL were enriched in functions associated to phagocytosis, such as the "Endocytosis" pathway and the "Early, late and recycling endosomes" cellular components (Extended Data Fig. 5h and Supplementary Table). Specifically, key genes of the phagocytic machinery were upregulated in the EVL tissue compared to progenitor cells, as rab7[24] (essential for phagosome-lysosome fusion), waslb[25] (n-wasp, involved in phagocytic cup formation), dynamin-2[26] (important for phagosome formation and closure), and other relevant players (including rabac1, pld1, asap2, EhVps32, cyth1, wipfh2, iqsec1). Surprisingly, multiple terms related to innate immune functions and repair response were also enriched among EVL upregulated genes (Extended Data Fig. 5h and Supplementary Table), suggesting a possible immuno-protective role of the surface epithelium in the early embryo beyond a phagocytic clearance function.

Epithelial phagocytosis was also observed in embryonic cell aggregates that self-organize and form an outer surface epithelium (Extended data Fig. 6a), supporting a primordial physiological tissue clearance activity mediated by epithelial cells. To evaluate the evolutionary conservation of epithelial uptake of apoptotic cells in early mammalian development, we further investigated apoptotic cell dynamics in mouse embryos. Time-lapse imaging of mouse blastocysts revealed endogenous apoptotic events of cells being extruded into the blastocyst cavity and later uptaken by the trophoblast, the embryonic surface epithelium of the mouse blastula (Extended Data Fig. 6b,b´,c, Supplementary Video 7). Similarly, apoptotic mouse embryonic stem cells transplanted into the blastocyst cavity were mostly uptaken by trophoblast cells (Extended Data Fig. 6d-g, Supplementary Video 7). Moreover, we transferred lipid-coated glass spheres as surrogate apoptotic targets into the blastocyst cavity, further confirming that uptake by trophoblast cells is dependent on the presence of PS on the target surface, comparable to epithelial clearance in zebrafish embryos (Fig. 1i-j and Extended Data Fig. 6h). In addition, a gene ontology enrichment analysis of genes specifically upregulated in trophoblast compared to inner cell mass from public RNASeq data[27] of pre-implantation mouse blastocysts revealed terms in common with zebrafish EVL, such as "endocytosis" and "immune-related" functions (Extended Data Fig. 5i and Supplementary Table). Of note, the presence of similar enriched functions was documented for human trophectoderm[28] (Supplementary Table). Altogether, these results suggest that the apoptotic phagocytic capacity of the surface embryonic epithelium is conserved in mammals.

A key aspect of epithelial phagocytosis is the restricted spatial exploration range of epithelial cells for apoptotic target search and capture, given their embedding in the epithelial tissue and their non-motile character. In comparison, professional phagocytes have migratory abilities relevant for efficient target encounter and uptake[10]. Interestingly, quantitative *in vivo* tracking of single apoptotic Bax^{+} cells revealed that they move with fast speed ($<v>$=8.3 +/- 0.2 µm/min), showing peak velocities of up to 30.1 +/- 1.5 µm/min (Fig. 2a-e, Supplementary Video 8), comparable to the speed reached by fast amoeboid migrating cells in 3D tissues[29]. In contrast, neighbouring live cells move at slower speed ($<v>$=1.8 +/- 0.1 µm/min) (Fig. 2a-e, Supplementary Video 8) and showed directional motility as part of their gastrulation movements to the vegetal pole of the embryo, while apoptotic cells moved non-directionally (Fig. 2b,c,f, Supplementary Video 8). Surprisingly, we found that phases of fast apoptotic movement were correlated with an accumulation of external F-actin, polarized at the apoptotic cell rear and opposite to its movement direction (Fig. 2a,g,h, Extended Data

Fig. 7a,b, Supplementary Videos 8 and 9). This observation indicated the presence of a non-autonomous actin network that is formed from surrounding embryonic cells in the blastula. Epithelium-specific staining revealed that polarized actin accumulations are formed by epithelial cells in a contact-dependent manner upon interaction with apoptotic cells (Extended Data Fig. 7c). Single cell staining of epithelial cells allowed to identify the formation of thin elongated protrusions that extended from the basal epithelial surface and were coordinated with apoptotic movement (Fig. 2i, Extended Data Fig. 7d, Supplementary Video 10), while these protrusions were not observed to form from live neighbouring cells. Protrusions showed a strong actin enrichment and retrograde actin flow in the protrusion front (Extended data Fig. 7e-f), suggesting that actin polymerization is triggered specifically at the protrusion tip in contact with the apoptotic target surface and different from continuously active basal ruffles (Extended Data Fig. 3e,f, Supplementary Videos 5 and 10). Given the characteristic features of these epithelial protrusions such as their dynamic extension and retraction (Extended Data Fig. 7d, Supplementary Video 10), and close physical association with motile apoptotic targets, we termed these protrusions "epithelial arms", reminiscent of an arm grabbing and moving an object. Quantification of the frequency of epithelial protrusion formation (61.6 +/- 9.7 arms/hour and 40.8 +/- 3.5 phagocytic cups/hour in the field of view, n=3 embryos) showed that arm protrusions occurred at comparable rates to phagocytic cup formation. Importantly, we also observed similar apoptotic motility and epithelial arm formation upon contact with endogenously dying cells (Extended Data Fig. 8a,b and Supplementary Video 1 and 11), and during induced apoptosis via Caspase8-ER^{T2} (Extended Data Fig. 8c-e) and mutant Topoisomerase-II expression (Extended Data Fig. 8f-h), or upon transplantation of apoptotic Jurkat T cells (Extended Data Fig. 8i, Supplementary Video 12). Equally to phagocytic uptake, arms and motility did not depend on the presence of a high number of apoptotic particles, as observed when few UV irradiated cells are transplanted into the embryo (Extended Data Fig. 8j, Supplementary Video 12). These results indicate that actin-based epithelial arms are formed in close association with apoptotic cells during phases of fast apoptotic motility, suggesting a mechanistic link between apoptotic cell motility and epithelial protrusion formation.

The coordination between epithelial arms and apoptotic motility raised different possible interaction mechanisms (Fig. 3a,b): 1) apoptotic cells are autonomously motile, as suggested previously for other apoptotic cells[30,31], and epithelial arms are associated with them via a run-and-chase mechanisms; or 2) apoptotic cells have no intrinsic motility and epithelial arms are actively involved in propelling apoptotic targets. To distinguish between these possibilities, we first analysed F-actin and Myosin II dynamics in single motile apoptotic cells *in vivo*. Both F-actin and Myosin II showed static intracellular localization patterns with an absence of cell surface protrusions or specific cortical localizations in apoptotic cells (Extended Data Fig. 9a,b, Supplementary Videos 9 and 12), suggesting that actin-based polymerization or Myosin II-mediated contractility in the apoptotic cell are not underlying its motility. Co-expression of Bax with dominant negative forms of proteins that control actomyosin-dependent motility, like the Rho GTPases[32] Rac1and RhoA or its downstream target Rock1, further did not affect apoptotic cell speed, nor the presence of actin arms or the ability of phagocytic uptake by epithelial cells (Extended Data Fig. 9c,d), supporting that apoptotic cells do not have autonomous motility. Injection of AnnexinV inside the embryo to coat PS on the surface of apoptotic cells blocked their motility and arm formation (Extended Data Fig. 9e), indicating that PS recognition is required to promote apoptotic motility associated with epithelial arm formation. In agreement, global epithelial-specific actin staining revealed that apoptotic motility was always associated with polarized actin enrichments in contact with the apoptotic cell rear (n=59/59 motile cells, 6 embryos; Extended Data Fig. 9f,g and Supplementary Video 12), supporting that apoptotic motility is specifically driven by epithelial arm protrusion. In contrast with specific interferences in apoptotic cells, ubiquitous expression of dnRac1 in the whole embryo blocked apoptotic cell motility and the formation of dynamic epithelial arms together with phagocytic target uptake (Fig. 3c-e, Extended Data Fig. 9h and Supplementary Video 13). This result further supports that Rac1 activity

is specifically required in epithelial cells for the formation of epithelial arms and that apoptotic cell motility is actively established by basal epithelial arm protrusions. Moreover, *ex vivo* 3D co-cultures of apoptotic and live cells under conditions in which epithelial tissue formation is absent, showed that apoptotic cells did not acquire motility or polarized F-actin accumulations (Extended Data Fig. 9i). To directly test if epithelial arms can exert mechanical forces to push apoptotic cells *in vivo*, we transferred surrogate apoptotic targets into the embryo as a source of objects with no intrinsic motility. Interestingly, PS^+ targets moved similarly to apoptotic cells with phases of high speed (Fig. 3f-h and Supplementary Video 13), and contact-dependent formation of epithelial actin-rich arms (Fig. 3f). In contrast, in PS^- targets this motility was absent (Fig. 3g-h). These data support that epithelial arms can actively push apoptotic fragments by actin polymerization-based protrusion forces generated locally at the apoptotic target surface. Epithelial cells thus establish two types of Rac1 dependent actin-based protrusions (Fig. 3a), epithelial arms and phagocytic cups, which promote apoptotic target movement by mechanical pushing and phagocytic uptake, respectively.

To identify molecular mechanisms underlying the formation of phagocytic epithelial cups versus epithelial arm protrusions, we performed an interference approach targeted at specific actin polymerization regulators. Using CK-666 as a pharmacological inhibitor of the Arp2/3 complex, which nucleates branched actin polymerization, blocked both the formation of epithelial arms and associated apoptotic cell motility, as well as epithelial phagocytic cups and target uptake (Fig. 3i-k,n and Supplementary Video 13). In contrast, SMIFH2, a specific inhibitor of Formin proteins that nucleate linear actin filaments, impaired only phagocytic uptake without affecting epithelial arm formation or apoptotic cell movement (Fig. 3k-n and Supplementary Video 13). Thus, epithelial phagocytic cup formation requires both Arp2/3 and Formin activity, while extended epithelial arm protrusions primarily depend on Arp2/3 network branching activity. Considering the generation of active pushing forces and involved actin nucleation factors, epithelial arms resemble actin comets[33], actin-rich structures that promote fast intracellular pushing of bacteria, with the difference that epithelial arms are able to propel large extracellular objects.

At the global tissue scale, epithelial arm pushing resulted in a wide dispersal of apoptotic targets along the epithelial surface before uptake (Fig. 4a), compared to a minor dispersal observed in the absence of epithelial arms (via interference with Rac1 or Arp2/3). Mean square displacement (MSD) analysis of the apoptotic cell paths showed that this spreading is created by a persistent random walk of each apoptotic particle (Fig. 4b), consisting in periods of fast and directional apoptotic motility during epithelial arm contacts and randomized directional changes upon consecutive contacts with multiple epithelial arms (Fig. 4c,d and Supplementary Video 14). The dynamic path of an apoptotic cell in the tissue therefore emerges by the collective mechanical action of multiple epithelial cells. This allows apoptotic cells to travel long distances before uptake ($<d>$=437 +/- 49 μm), which promotes their uptake at distant locations in the epithelial tissue further away from the site they were dying (as visualized by a map of phagocytic uptake events, Fig. 4e), establishing a mechanical cooperation between epithelial cells. Along its path, each apoptotic cell faces multiple epithelial cells (Fig. 4f), engaging more epithelial phagocytes for participation in the clearance tasks. Similar to the recruitment of motile professional phagocytes during apoptotic clearance upon tissue damage[34], active protrusion-mediated spreading resembles an inversion of the process in which targets are moving around multiple non-motile phagocytic cells to promote collective uptake. To visualize the impact of protrusion-mediated spreading from a localized region of apoptotic cells, we mimicked an apoptotic damage source by transplanting a defined number of apoptotic cells underneath the EVL tissue of an acceptor embryo (Supplementary Video 14). Prior to uptake, transplanted apoptotic particles were pushed and actively dispersed by epithelial arms, increasing their effective spreading area by $2x10^4$ μm^2 in 1 h, equivalent to an area covered by about 22 epithelial cells (Fig. 4g). Importantly, single endogenously dying cells were also uptaken by multiple epithelial cells (Fig. 1a, Supplementary Videos 1 and 2). Together, epithelial arm protrusions promote apoptotic cell dispersal

via mechanical target pushing underneath the epithelial layer. This mechanism ensures increased encounter rates of apoptotic targets with epithelial cells and the cooperative participation of multiple epithelial cells in the clearance process, a process we refer to as mechanical load-sharing (sharing the uptake load by mechanically distributing objects before uptake).

To understand how active dispersal and cooperative uptake could influence apoptotic target clearance dynamics, we performed computational and theoretical modelling. First, we implemented Monte Carlo simulations of apoptotic target spreading, parameterized by the pushing probability p_v, the speed v, and pushing period τ, and concomitant target uptake by epithelial cells, each of lateral extent L. Target uptake occurs with probability p_{up} and is limited by the maximum uptake capacity of individual epithelial cells, defined as a variable parameter N_{max} (Extended Data Fig. 10a). Such a limit in phagocytic uptake has been documented in professional phagocytes[35,36]. Particularly, epithelial cells can have both physical and biochemical limitations in the phagocytic uptake capacity, for instance caused by the maximal extension a phagocytic cell can undergo before epithelial tissue integrity is lost, or the exhaustion of the phagocytic uptake machinery (as actin is used for cell-cell junction maintenance, see Extended Data Fig. 3b´-b´´´). Assuming a localized initial accumulation of apoptotic targets N_{target}, we analysed target dispersal and spatio-temporal uptake characteristics in the epithelium. Simulation kymographs showed a characteristic dispersal of apoptotic targets with an effective diffusion constant D_{eff} (Fig.4 h,i (bottom) and Supplementary Note). Spreading enables apoptotic target uptake within an expanding area of the epithelium in which cells have not reached their uptake limit N_{max} yet (Fig.4 h,i (top)). Importantly, faster target dispersal decreased total tissue clearance time t_{clear} (measured as the time to complete clearance of the whole apoptotic mass) (Fig. 4j), with t_{clear} varying as $\sim 1/v^2$ as obtained from analytical derivation of the total clearance time (Supplementary Note). Target dispersal via the process of collective mechanical load-sharing reduces the overall clearance time by engaging multiple epithelial cells in the clearance activity. This mechanism is highly effective even under conditions when an increased number of localized targets (N_{target}) has to be cleared. It does so by promoting target uptake by an increased epithelial tissue area to circumvent local phagocytic saturation, with t_{clear} varying as $\sim(N_{target}/N_{max})^2$ (Fig. 4k and Extended Data Fig. 10b). Overall, our modelling supports that mechanical target spreading and cooperative clearance profoundly extends the limited spatial exploration and uptake range of individual non-motile epithelial cells to optimize tissue clearance.

To directly assess epithelial uptake efficiency in the physiological *in vivo* context, we performed cell transplantations of a large amount of apoptotic Jurkat cell targets (282 +/- 22, Extended Data Fig. 11a,b). Quantitative analysis of the number of ingested particles in single epithelial cells showed a temporal increase until a characteristic plateau was reached after about 140 min of uptake (2.8 +/- 0.3 targets, Extended Data Fig. 11c,d). This plateau emerged albeit still having apoptotic targets available in contact with the basal epithelial surface (Extended Data Fig. 11c,e), supporting that epithelial cells have an intrinsic physiological limit in their uptake capacity N_{max}. Spatio-temporal analysis of phagocytic uptake dynamics revealed that neighbouring epithelial cells located outside of saturated areas in the epithelium engaged in the clearance process over time (Extended Data Fig. 11f), promoting target uptake by an increased number of phagocytes. The efficiency of active target dispersal for tissue clearance further becomes evident when measuring the maximum uptake volume V_{max} per epithelial cell (V_{max}=1200 +/- 60 μm^3, Fig. 11g,h). Given an average volume of an apoptotic cell V_{target}= 2400 +/- 200 μm^3, a single epithelial cell will only be able to clear about 0.5 apoptotic cells before saturation. This makes mechanical target dispersal relevant for both low and high numbers of apoptotic cells to ensure rapid and efficient clearance by engaging more phagocytes in the clearance process. Together, our data provide direct experimental support that epithelial phagocytes have a restricted phagocytic uptake range. We show that apoptotic cell movement via active target dispersal enables to increase the number of participating phagocytes in the tissue clearance process, establishing a mechanical cooperation between epithelial cells. Similarly, motile

professional phagocytes are often operating in groups, with the number of recruited phagocytes being proportional to the mass that needs to be cleared for improving uptake efficiency[34,37,38].

Our work proposes a new evolutionarily conserved function for epithelial tissues as efficient scavengers of apoptotic cells in the earliest stages of vertebrate embryogenesis, relevant for error correction and developmental robustness. This scavenging system operates both at low and high levels of cell death occurring in the embryo, becoming relevant for tissue homeostasis in the presence of sporadic cell death and when failures involve large regions and compromise embryo survival, emulating roles of the immune system in adult tissues. Epithelial phagocytosis was also shown to regulate tissue homeostasis and inflammation in specific organs of the adult organisms in which phagocytic load is shared with professional phagocytes[18,39] and in immune-privileged tissues such as the retina and the testis[40]. Here we show that during early embryonic development epithelial cells specialize to perform phagocytic immune functions in the complete absence of immune cells. At later developmental stages, once differentiation of professional phagocytes occurs, these cells can share their phagocytic tasks with other cell types, both mesenchymal or epithelial[41-44]. The presence of an epithelial protection mechanism in other early embryonic contexts should be further explored, as phagocytic functions during development were also identified in invertebrates[45-48].

While chemical cooperation between cells has been well documented, mechanical cooperation as a physiological tissue function remains only poorly understood. Overall, our results support that active mechanical distribution of apoptotic targets promotes phagocytic cooperation among epithelial cells. This can ensure a rapid and efficient clearance of apoptotic targets through a division of labour by engaging multiple epithelial cells in a cooperative manner to perform phagocytic uptake activity. We identify that Formins and Arp2/3 are involved in generating two different types of basal epithelial protrusions required for mechanical cell cooperation. These actin regulators have also been implicated in phagocytic protrusion plasticity in macrophages[49]. It will be interesting to explore in future studies how both molecular and biophysical features of apoptotic targets and epithelial cells influence the type of protrusion formation. Mechanical cell cooperation as a new mechanism to improve phagocytic clearance can have broad relevance in pathological and physiological conditions in which phagocytic uptake plays a central role as in homeostatic cell turnover[50,51] and tissue inflammation[52].

Acknowledgements

We would like to thank Thomas Graf, Ben Lehner and Vivek Malhotra for discussions and critical reading of the manuscript. Q.T.-R. acknowledges a grant funded by "The Ministerio de Ciencia, Innovación y Universidades and Fondo Social Europeo (FSE)" (PRE2018-084393). M.I. acknowledges funding from the European Research Council (ERC) under the European Union's Horizon 2020 research and innovation program (ERC-StG-LS2-63759) and the Spanish Ministry of Economy and Competitiveness (BFU2014-55076-P). S.W. acknowledges support through the Spanish Ministry of Economy and Competitiveness via MINECO's Plan Nacional (BFU2017-86296-P), through the "Severo Ochoa" program for Centres of Excellence in R&D (SEV-2015-0522), from Fundació Privada Cellex, Fundación Mig-Puig and from Generalitat de Catalunya through the CERCA program and LaserLab (No 654148).V.R. acknowledges support from the Spanish Ministry of Economy and Competitiveness through the Program "Centro de Excelencia Severo Ochoa 2013-2017", the CERCA Programme/ Generalitat de Catalunya, MINECO's Plan Nacional (BFU2017-86296-P) and support from the CRG Core Facilities for Genomics, Biomolecular Screening and Protein Technologies, Flow Cytometry and Advanced Light Microscopy.

Author contributions

E.H. designed research, performed experiments and analyzed data. H.-M.H. contributed to *in vivo* experiments and cell tracking. Q.T.-R. contributed to *in vivo* imaging and *in vitro* experiments. S.J.-

D. supported cloning and mRNA injections. C.W. performed sequencing analysis. M.M.-C. contributed to mouse blastocyst experiments. M.I. supervised C.W. and M.M.-C. and performed sequencing analysis. A.C.-J. performed theoretical modeling. S.W. analyzed data and performed Monte Carlo simulations. V.R. designed research, performed data analysis and supervised the project. E.H. and V.R. wrote the manuscript with the contribution of all authors.

Reprints and permissions information is available at www.nature.com/reprints.
The authors declare no competing interest.
Correspondence and requests for materials should be addressed to esteban.hoijman@crg.eu, Stefan.Wieser@icfo.eu, verena.ruprecht@crg.eu

References

1 Schneider, I. & Ellenberg, J. Mysteries in embryonic development: How can errors arise so frequently at the beginning of mammalian life? *PLoS Biol* 17, e3000173, doi:10.1371/journal.pbio.3000173 (2019).

2 Bolton, H. *et al.* Mouse model of chromosome mosaicism reveals lineage-specific depletion of aneuploid cells and normal developmental potential. *Nat Commun* 7, 11165, doi:10.1038/ncomms11165 (2016).

3 Artus, J., Kang, M., Cohen-Tannoudji, M. & Hadjantonakis, A. K. PDGF signaling is required for primitive endoderm cell survival in the inner cell mass of the mouse blastocyst. *Stem Cells* 31, 1932-1941, doi:10.1002/stem.1442 (2013).

4 Zhong, J. X., Zhou, L., Li, Z., Wang, Y. & Gui, J. F. Zebrafish Noxa promotes mitosis in early embryonic development and regulates apoptosis in subsequent embryogenesis. *Cell Death Differ* 21, 1013-1024, doi:10.1038/cdd.2014.22 (2014).

5 Claveria, C., Giovinazzo, G., Sierra, R. & Torres, M. Myc-driven endogenous cell competition in the early mammalian embryo. *Nature* 500, 39-44, doi:10.1038/nature12389 (2013).

6 Akieda, Y. *et al.* Cell competition corrects noisy Wnt morphogen gradients to achieve robust patterning in the zebrafish embryo. *Nat Commun* 10, 4710, doi:10.1038/s41467-019-12609-4 (2019).

7 Vanneste, E. *et al.* Chromosome instability is common in human cleavage-stage embryos. *Nat Med* 15, 577-583, doi:10.1038/nm.1924 (2009).

8 Greco, E., Minasi, M. G. & Fiorentino, F. Healthy Babies after Intrauterine Transfer of Mosaic Aneuploid Blastocysts. *N Engl J Med* 373, 2089-2090, doi:10.1056/NEJMc1500421 (2015).

9 Fuchs, Y. & Steller, H. Programmed cell death in animal development and disease. *Cell* 147, 742-758, doi:10.1016/j.cell.2011.10.033 (2011).

10 Elliott, M. R. & Ravichandran, K. S. The Dynamics of Apoptotic Cell Clearance. *Dev Cell* 38, 147-160, doi:10.1016/j.devcel.2016.06.029 (2016).

11 Guillot, C. & Lecuit, T. Mechanics of epithelial tissue homeostasis and morphogenesis. *Science* 340, 1185-1189, doi:10.1126/science.1235249 (2013).

12 Duszyc, K., Gomez, G. A., Schroder, K., Sweet, M. J. & Yap, A. S. In life there is death: How epithelial tissue barriers are preserved despite the challenge of apoptosis. *Tissue Barriers* 5, e1345353, doi:10.1080/21688370.2017.1345353 (2017).

13 Oltvai, Z. N., Milliman, C. L. & Korsmeyer, S. J. Bcl-2 heterodimerizes in vivo with a conserved homolog, Bax, that accelerates programmed cell death. *Cell* 74, 609-619, doi:10.1016/0092-8674(93)90509-o (1993).

14 Furniss, K. L. *et al.* Direct monitoring of the strand passage reaction of DNA topoisomerase II triggers checkpoint activation. *PLoS Genet* 9, e1003832, doi:10.1371/journal.pgen.1003832 (2013).

15 Palchaudhuri, R. *et al.* A Small Molecule that Induces Intrinsic Pathway Apoptosis with Unparalleled Speed. *Cell Rep* 13, 2027-2036, doi:10.1016/j.celrep.2015.10.042 (2015).

16 Slanchev, K. *et al.* The epithelial cell adhesion molecule EpCAM is required for epithelial morphogenesis and integrity during zebrafish epiboly and skin development. *PLoS Genet* 5, e1000563, doi:10.1371/journal.pgen.1000563 (2009).

17 Patel, P. C. & Harrison, R. E. Membrane ruffles capture C3bi-opsonized particles in activated macrophages. *Mol Biol Cell* 19, 4628-4639, doi:10.1091/mbc.E08-02-0223 (2008).
18 Juncadella, I. J. *et al.* Apoptotic cell clearance by bronchial epithelial cells critically influences airway inflammation. *Nature* 493, 547-551, doi:10.1038/nature11714 (2013).
19 Akhtar, N., Li, W., Mironov, A. & Streuli, C. H. Rac1 Controls Both the Secretory Function of the Mammary Gland and Its Remodeling for Successive Gestations. *Dev Cell* 38, 522-535, doi:10.1016/j.devcel.2016.08.005 (2016).
20 Nakaya, M., Kitano, M., Matsuda, M. & Nagata, S. Spatiotemporal activation of Rac1 for engulfment of apoptotic cells. *Proc Natl Acad Sci U S A* 105, 9198-9203, doi:10.1073/pnas.0803677105 (2008).
21 Schlam, D. *et al.* Phosphoinositide 3-kinase enables phagocytosis of large particles by terminating actin assembly through Rac/Cdc42 GTPase-activating proteins. *Nat Commun* 6, 8623, doi:10.1038/ncomms9623 (2015).
22 Jaumouille, V., Cartagena-Rivera, A. X. & Waterman, C. M. Coupling of beta2 integrins to actin by a mechanosensitive molecular clutch drives complement receptor-mediated phagocytosis. *Nat Cell Biol* 21, 1357-1369, doi:10.1038/s41556-019-0414-2 (2019).
23 Fadok, V. A. *et al.* Exposure of phosphatidylserine on the surface of apoptotic lymphocytes triggers specific recognition and removal by macrophages. *J Immunol* 148, 2207-2216 (1992).
24 Vieira, O. V. *et al.* Modulation of Rab5 and Rab7 recruitment to phagosomes by phosphatidylinositol 3-kinase. *Mol Cell Biol* 23, 2501-2514, doi:10.1128/mcb.23.7.2501-2514.2003 (2003).
25 Park, H. & Cox, D. Cdc42 regulates Fc gamma receptor-mediated phagocytosis through the activation and phosphorylation of Wiskott-Aldrich syndrome protein (WASP) and neural-WASP. *Mol Biol Cell* 20, 4500-4508, doi:10.1091/mbc.E09-03-0230 (2009).
26 Marie-Anais, F., Mazzolini, J., Herit, F. & Niedergang, F. Dynamin-Actin Cross Talk Contributes to Phagosome Formation and Closure. *Traffic* 17, 487-499, doi:10.1111/tra.12386 (2016).
27 Deng, Q., Ramskold, D., Reinius, B. & Sandberg, R. Single-cell RNA-seq reveals dynamic, random monoallelic gene expression in mammalian cells. *Science* 343, 193-196, doi:10.1126/science.1245316 (2014).
28 Petropoulos, S. *et al.* Single-Cell RNA-Seq Reveals Lineage and X Chromosome Dynamics in Human Preimplantation Embryos. *Cell* 167, 285, doi:10.1016/j.cell.2016.08.009 (2016).
29 Ruprecht, V. *et al.* Cortical contractility triggers a stochastic switch to fast amoeboid cell motility. *Cell* 160, 673-685, doi:10.1016/j.cell.2015.01.008 (2015).
30 van Ham, T. J., Kokel, D. & Peterson, R. T. Apoptotic cells are cleared by directional migration and elmo1- dependent macrophage engulfment. *Curr Biol* 22, 830-836, doi:10.1016/j.cub.2012.03.027 (2012).
31 Yamaguchi, Y. *et al.* Live imaging of apoptosis in a novel transgenic mouse highlights its role in neural tube closure. *J Cell Biol* 195, 1047-1060, doi:10.1083/jcb.201104057 (2011).

32 Heasman, S. J. & Ridley, A. J. Mammalian Rho GTPases: new insights into their functions from in vivo studies. *Nat Rev Mol Cell Biol* 9, 690-701, doi:10.1038/nrm2476 (2008).
33 Welch, M. D., Iwamatsu, A. & Mitchison, T. J. Actin polymerization is induced by Arp2/3 protein complex at the surface of Listeria monocytogenes. *Nature* 385, 265-269, doi:10.1038/385265a0 (1997).
34 Lammermann, T. *et al.* Neutrophil swarms require LTB4 and integrins at sites of cell death in vivo. *Nature* 498, 371-375, doi:10.1038/nature12175 (2013).
35 Zent, C. S. & Elliott, M. R. Maxed out macs: physiologic cell clearance as a function of macrophage phagocytic capacity. *FEBS J* 284, 1021-1039, doi:10.1111/febs.13961 (2017).
36 Armitage, E. L., Roddie, H. G. & Evans, I. R. Overexposure to apoptosis via disrupted glial specification perturbs Drosophila macrophage function and reveals roles of the CNS during injury. *bioaRxiv*, doi:https://doi.org/10.1101/2020.03.04.977546 (2020).
37 Voelz, K., Gratacap, R. L. & Wheeler, R. T. A zebrafish larval model reveals early tissue-specific innate immune responses to Mucor circinelloides. *Dis Model Mech* 8, 1375-1388, doi:10.1242/dmm.019992 (2015).
38 Evans, I. R., Ghai, P. A., Urbancic, V., Tan, K. L. & Wood, W. SCAR/WAVE-mediated processing of engulfed apoptotic corpses is essential for effective macrophage migration in Drosophila. *Cell Death Differ* 20, 709-720, doi:10.1038/cdd.2012.166 (2013).
39 Lee, C. S. *et al.* Boosting Apoptotic Cell Clearance by Colonic Epithelial Cells Attenuates Inflammation In Vivo. *Immunity* 44, 807-820, doi:10.1016/j.immuni.2016.02.005 (2016).
40 Penberthy, K. K., Lysiak, J. J. & Ravichandran, K. S. Rethinking Phagocytes: Clues from the Retina and Testes. *Trends Cell Biol* 28, 317-327, doi:10.1016/j.tcb.2018.01.004 (2018).
41 Zhu, Y. *et al.* Migratory Neural Crest Cells Phagocytose Dead Cells in the Developing Nervous System. *Cell* 179, 74-89 e10, doi:10.1016/j.cell.2019.08.001 (2019).
42 Wood, W. *et al.* Mesenchymal cells engulf and clear apoptotic footplate cells in macrophageless PU.1 null mouse embryos. *Development* 127, 5245-5252 (2000).
43 Ellis, S. J. *et al.* Distinct modes of cell competition shape mammalian tissue morphogenesis. *Nature* 569, 497-502, doi:10.1038/s41586-019-1199-y (2019).
44 Rasmussen, J. P., Sack, G. S., Martin, S. M. & Sagasti, A. Vertebrate epidermal cells are broad-specificity phagocytes that clear sensory axon debris. *J Neurosci* 35, 559-570, doi:10.1523/JNEUROSCI.3613-14.2015 (2015).
45 Fazeli, G., Stetter, M., Lisack, J. N. & Wehman, A. M. C. elegans Blastomeres Clear the Corpse of the Second Polar Body by LC3-Associated Phagocytosis. *Cell Rep* 23, 2070-2082, doi:10.1016/j.celrep.2018.04.043 (2018).
46 Gumienny, T. L., Lambie, E., Hartwieg, E., Horvitz, H. R. & Hengartner, M. O. Genetic control of programmed cell death in the Caenorhabditis elegans hermaphrodite germline. *Development* 126, 1011-1022 (1999).
47 Nakanishi, N., Sogabe, S. & Degnan, B. M. Evolutionary origin of gastrulation: insights from sponge development. *BMC Biol* 12, 26, doi:10.1186/1741-7007-12-26 (2014).

48 Silva, J. R. The onset of phagocytosis and identity in the embryo of Lytechinus variegatus. *Dev Comp Immunol* 24, 733-739, doi:10.1016/s0145-305x(00)00028-8 (2000).
49 Davidson, A. J. & Wood, W. Macrophages Use Distinct Actin Regulators to Switch Engulfment Strategies and Ensure Phagocytic Plasticity In Vivo. Cell Rep 31, 107692, doi:10.1016/j.celrep.2020.107692 (2020).
50 Arandjelovic, S. & Ravichandran, K. S. Phagocytosis of apoptotic cells in homeostasis. *Nat Immunol* 16, 907-917, doi:10.1038/ni.3253 (2015).
51 Lim, J. J., Grinstein, S. & Roth, Z. Diversity and Versatility of Phagocytosis: Roles in Innate Immunity, Tissue Remodeling, and Homeostasis. *Front Cell Infect Microbiol* 7, 191, doi:10.3389/fcimb.2017.00191 (2017).
52 Arienti, S., Barth, N. D., Dorward, D. A., Rossi, A. G. & Dransfield, I. Regulation of Apoptotic Cell Clearance During Resolution of Inflammation. *Front Pharmacol* 10, 891, doi:10.3389/fphar.2019.00891 (2019).

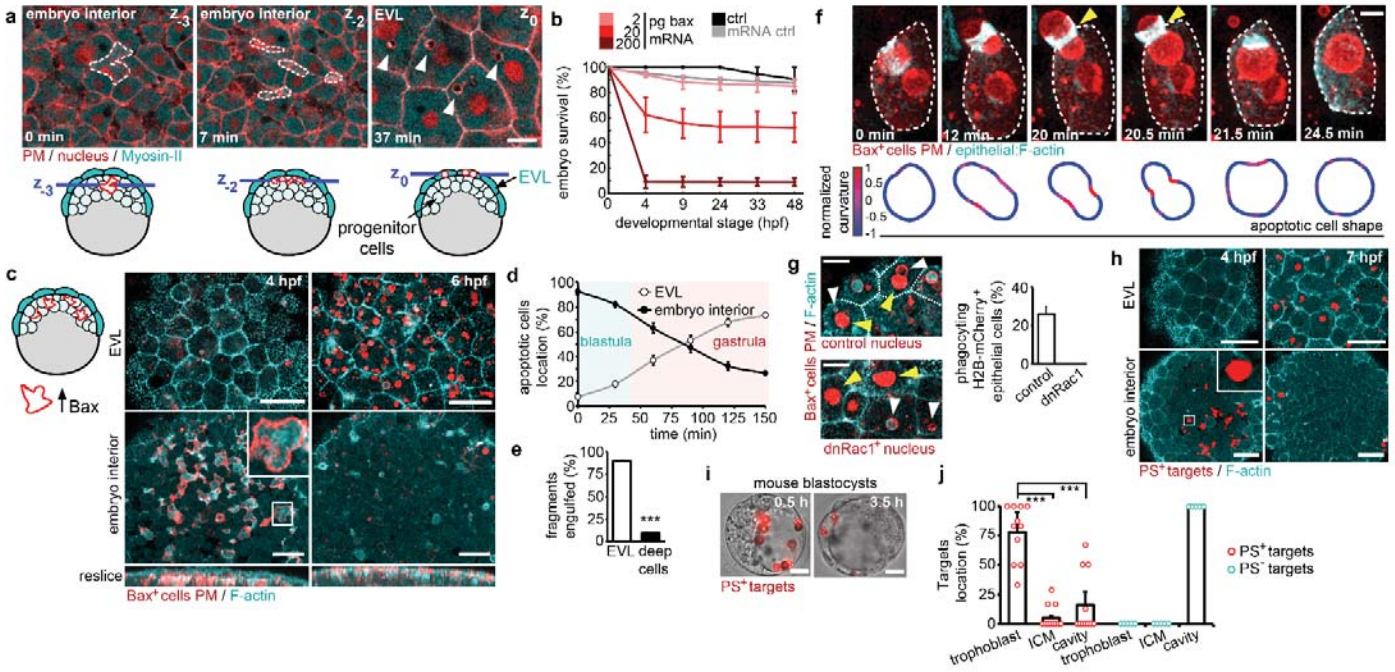

Fig. 1. The embryonic surface epithelium performs efficient phagocytic clearance of apoptotic cells. (**a**) Endogenous cell death dynamics of a single progenitor cell (dashed lines) showing cell shape loss (0 min), fragmentation (7 min) and epithelial uptake (37 min) in a Tg(Myl12.1-eGFP) embryo co-expressing Lyn-tdTomato (plasma membrane, PM) and H2A-mCherry (nucleus). The imaging plane (z) was changing over time. Arrowheads indicate uptaken particles inside the enveloping epithelial layer (EVL). (**b**) Embryo survival curves in unperturbed wildtype embryos (ctrl) and upon mosaic injection of mRNA for a plasma membrane marker only (lyn-tdTomato, mRNA ctrl) or together with varying levels of bax mRNA (2-200 pg). 3 independent experiments with at least 100 embryos per condition. (**c**) Representative images of Tg(actb1:Lifeact-GFP) embryos with mosaic co-expression of Bax (Bax$^+$ cells, from 2pg mRNA injection leading to 48.6 +/- 6.3 apoptotic cells in a field of view of 2.06 +/- 0.16 x10^6 um^3, n=5 embryos) and Lyn-tdTomato showing the uptake of these cells within the EVL versus clearance of the embryo interior over time. (**d**) Quantitative epithelial clearance dynamics of Bax$^+$ cells (n=6 embryos). (**e**) Engulfment of apoptotic particles by the EVL or by progenitor cells in the embryo interior at 6 hpf. (**f**) Max z-projection of a single epithelial cell (dashed line) expressing Lifeact-GFP by a krt18 promoter during the in vivo phagocytic uptake of an apoptotic Bax$^+$ cell. Lower panel: apoptotic cell shape changes during phagocytosis indicated by color-coded normalized curvatures. Arrowheads (upper panels) indicate regions of high apoptotic cell deformation associated with epithelial actin enrichment. (**g**) Rac1 involvement in epithelial phagocytic uptake analysed in embryos with two mosaic cell populations: 1) cells expressing H2A-mCherry only (upper panel) or co-expressing dnRac1 (lower panel) and 2) Bax$^+$ cells. White arrowheads indicate uptaken apoptotic fragments in the EVL. Yellow arrowheads indicate red nuclear staining. Quantification of uptake rates (right). Note that epithelial cells expressing dnRac1 (lower panel) are not able to phagocyte particles compared to control cells (upper panel) (n=6 embryos). Dashed lines indicate EVL cell contours. (**h**) Epithelial clearance of surrogate apoptotic targets formed by lipid aggregates containing PS, PC and TexasRed-DHPE (PS$^+$ targets) injected into Tg(actb1:Lifeact-GFP) embryos. Inset shows a magnified view of a PS$^+$ surrogate apoptotic target. (**i**) Clearance of PS$^+$ surrogate apoptotic targets (glass spheres coated with PS, PC and TexasRed-DHPE) injected in the mouse blastocyst cavity by trophoblast cells and (**j**) quantification of target localizations 3.5 h after injection. h: hours after injection (4 experiments, n=11 embryos for PS$^+$ targets

and 5 embryos for PS^- targets). Scale bars: 20 μm (a, g, i) and 50 μm (c,h) μm. hpf, hours post fertilization. Mean and standard errors are shown. *** $p<0.0001$.

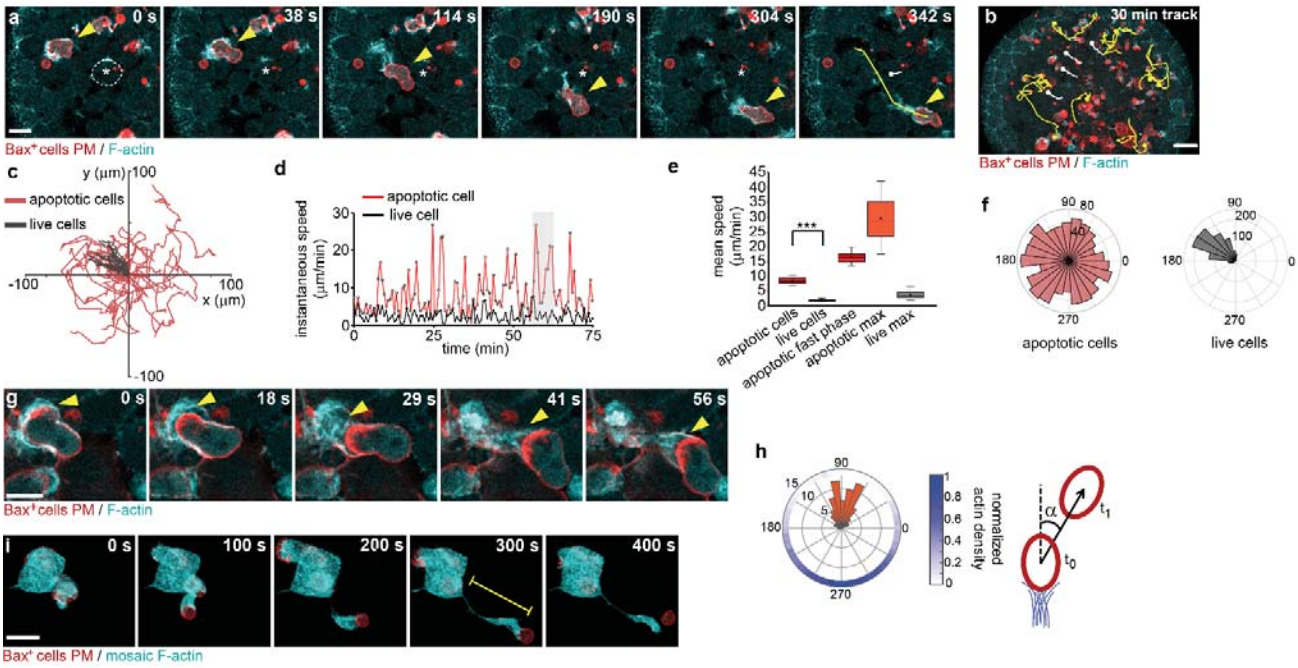

Fig. 2. Apoptotic cells acquire fast motility associated to actin-based epithelial arm protrusions. (**a**) Fast motility of a single apoptotic Bax$^+$ cell (arrowhead) compared to a live progenitor cell (dashed line and asterisk) in a Tg(actb1:Lifeact-GFP) embryo. Yellow and white lines indicate total path lengths of apoptotic and live cells, respectively. (**b**) Examples of apoptotic (yellow lines) and live (white lines) cell motility during a period of 30 min from 3D in vivo tracking. (**c**) Representative x-y trajectories centred to the origin obtained from 3D cell tracking of apoptotic and live cells. (**d**) Instantaneous cell speed fluctuations of an apoptotic and a live cell. The grey region represents a phase of fast motility. (**e**) Mean instantaneous cell speeds calculated from 3D tracking (n=28/25 apoptotic/live cells). (**f**) Angle distribution of tracks for apoptotic and live cells (n=29/23 cells from 3 embryos). (**g**) High speed imaging of in vivo apoptotic movement dynamics of a single Bax$^+$ cell in a Tg(actb1:Lifeact-GFP) embryo. Arrowheads indicate the association with an external F-actin accumulation. (**h**) Angle histogram of cell movement directions (α, orange) between t_0 and t_1 (t_{lag}=60 s) and external F-actin localization (blue) at t_0 along a circle reflecting the apoptotic cell perimeter, indicating actin enrichment in contact with the rear surface of the cell (87 direction angle changes and density profiles from 15 cells and 3 embryos). Sketch of the data analysis (right). (**i**) Epithelial arm protrusion from the surface of a single epithelial cell labelled by mosaic expression of Lifeact-GFP. Yellow line indicates the length of the epithelial arm protrusion (45 µm). Scale bars: 20 µm (a,g), 50 µm (b) and 10 µm (i). Mean and standard error are shown. *** $p<0.0001$.

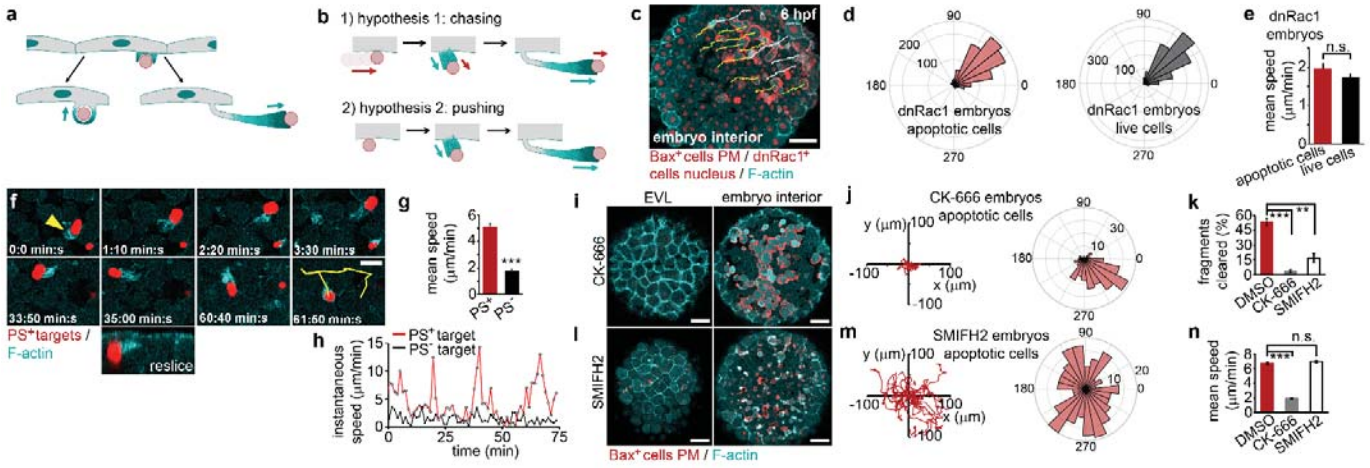

Fig. 3. Epithelial arms mechanically push apoptotic cells. (**a**) Epithelial cells show two types of actin-rich basal protrusions: phagocytic cups (left) and epithelial arms (right). (**b**) Two possible interaction mechanisms between epithelial arms and apoptotic cells: 1) apoptotic cells have autonomous motility and epithelial arm protrusions are chasing the apoptotic target; 2) apoptotic cells have no intrinsic motility and arms perform active pushing (lower panel). (**c,d**) Representative x-y trajectories obtained from 3D tracking of mosaic apoptotic Bax^{+} cells (yellow) and live cells (white) in embryos ubiquitously co-expressing dnRac1 (dnRac1+ cells) and H2a-mCherry (nucleus), and corresponding angle distributions (d). (**e**) Mean instantaneous cell speeds of apoptotic and live cells in dnRac1 expressing embryos (n=25/24 apoptotic/live cells; 4 embryos). (**f**) Motility of PS^{+} surrogate apoptotic targets in association with epithelial arms. Arrowhead indicates F-actin accumulation; yellow line outlines the total target path length over the indicated period. (**g**) Mean instantaneous speeds of surrogate targets (n=26 PS^{+} targets, 6 embryos; 23 PS^{-} targets, 5 embryos). (**h**) Instantaneous movement dynamics of lipid aggregates containing PS, PC and TexasRed-DHPE (PS+ targets) or omitting PS (PS^{-} targets). (**i-n**) Clearance of apoptotic cells in the presence of CK-666 or SMIFH2 inhibitors. Representative images (i,l), representative x-y trajectories (left) and angle distributions (right) for apoptotic cells (j,m), quantification of phagocytic epithelial clearance (k; n=6/5 embryos for CK-666/DMSO and n=4/4 embryos for SMIFH2/DMSO), and mean instantaneous speed (n; n=27/16 cells from N=3/3 embryos for CK-666/DMSO, and n=27/22 cells from n=3/5 embryos for SMIFH2/DMSO). All embryos are Tg(actb1:Lifeact-GFP). Scale bars: 50 μm (c,i,l) and 20 μm (f). Mean and standard error are shown. *** p<0.0001, ** p<0.005. n.s. not significant.

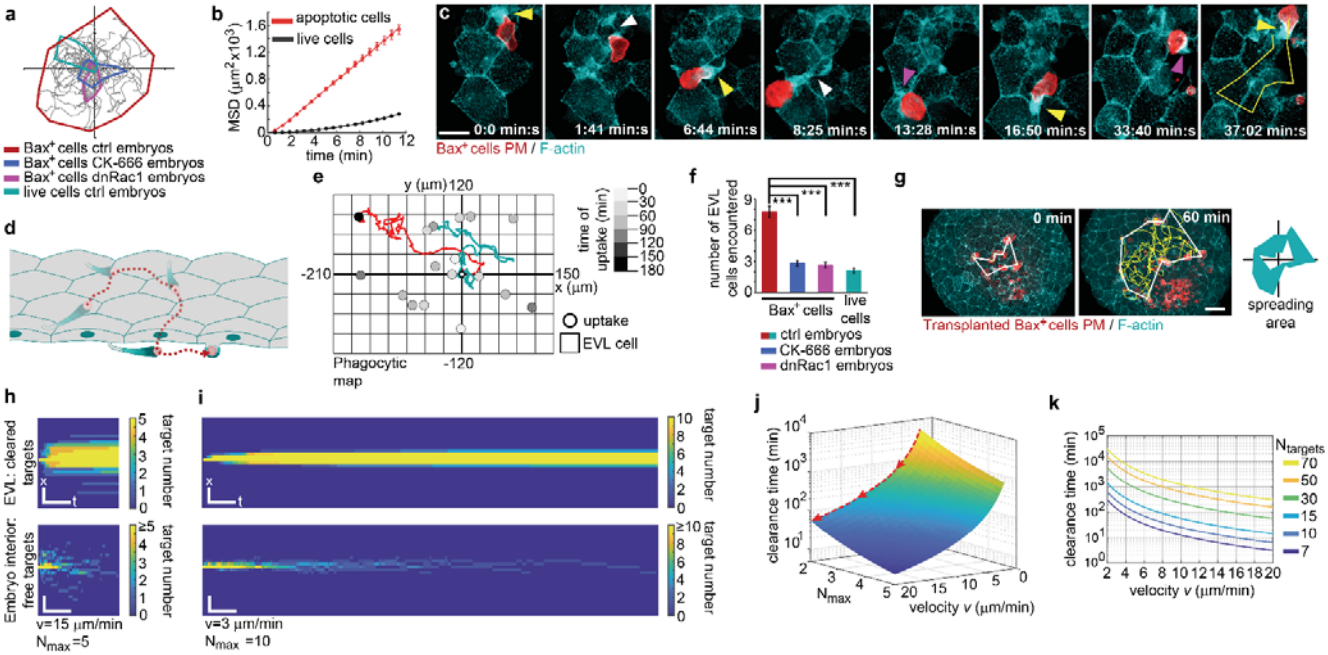

Fig. 4. Epithelial cells act cooperatively to promote apoptotic cell spreading for improving tissue clearance efficiency. (**a**) Spreading area of apoptotic cells in control, CK-666, and dnRac1 embryos, and of live cells in control embryos. (**b**) Mean square displacement (MSD) analysis of apoptotic versus live cells (n=29/23 cells), with apoptotic fragments showing a persistent random walk behaviour and live cells random motion with directional flow. (**c**) Sequential pushing events by multiple arm protrusions from different epithelial cells create a movement path of apoptotic cells along the epithelial layer (yellow line). Magenta arrowheads indicate F-actin accumulations upon new arm formation, yellow arrowheads show epithelial arms in the pushing phase and white arrowheads indicate thinning of arms upon retraction. Embryo is double mosaic for Bax^{+}/Lyn-tdTomato (PM) and Lifeact-GFP expression. (**d**) Schematic illustration of consecutive arm pushing creating an apoptotic movement path spanning multiple epithelial cells prior to phagocytic uptake. (**e**) Phagocytic uptake map over time indicating the x-y coordinates of single phagocytic events (grey circles) for individual apoptotic cells. Two representative paths (red and cyan) are shown. Each square of the grid represents an epithelial cell of the surface. The initial positions of the apoptotic cells were set at the origin (n=17 cells, 4 embryos). (**f**) Number of EVL cells encountered by individual apoptotic cells before uptake in control embryos (ctrl), or by apoptotic cells in CK-666 and dnRac1 embryos, and live cells in control embryos in an equivalent time period (n=17 cells, 4 embryos; see also cyan and red tracks in (e) for an example of EVL encounters during apoptotic cell traveling). (**g**) Representative images showing transplantation of Bax^{+} cells into a Tg(actb1:Lifeact-GFP) embryo. White lines outline the areas of cell dispersion over time. Yellow lines indicate apoptotic cell trajectories. The differential increase in the effective spreading area of apoptotic cells is indicated on the right. (**h,i**) Kymographs obtained from Monte Carlo simulations of apoptotic target cell spreading (bottom) and epithelial uptake (top) across a one-dimensional epithelial layer (x) over time (t) for high pushing speed v and low maximum uptake capacity N_{max} per epithelial cell (v=15 µm/min, N_{max}=5; h) or lower pushing rate and higher uptake capacity (v=3 µm/min, N_{max}=10; i). Scale bars: 25 min (t) and 100 µm (x). (**j**) Plot of clearance time versus N_{max} and target pushing velocity v for a total number of targets N_{target}=15. (**k**) Plot of clearance time versus pushing velocity for different N_{target} with N_{max}=4. Scale bars: 20 µm (c) and 50 µm (g). Mean and standard error are shown. *** p<0.0001.

Supplementary Information

Supplementary Information includes

- Extended data figures and legends 1 to 11
- Extended data table and legend
- Supplementary table legend
- Materials and methods
- Supplementary notes
- Captions for supplementary videos 1 to 14
- References

Extended data figures

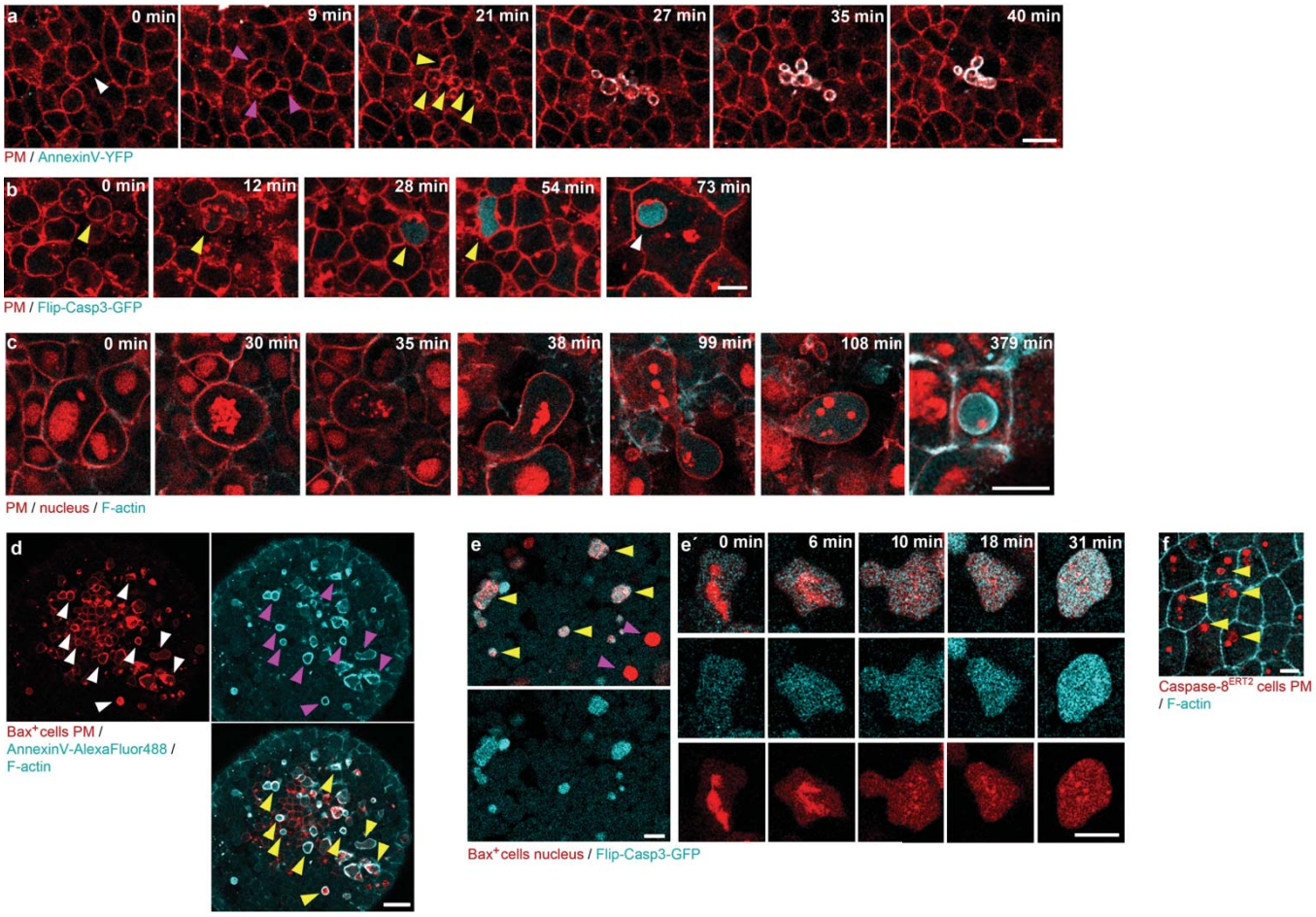

Extended Data Fig. 1. Endogenous and induced cell death events occur by apoptosis. (**a**) Endogenous cell (white arrowhead) undergoing shape loss (magenta arrowheads), fragmentation (yellow arrowheads) and PS exposure (27-40 min) as detected by ubiquitous expression of a secreted version of AnnexinV-YFP. (**b**) Caspase-3 activation dynamics in an endogenously dying cell (yellow arrowheads) as visualized by expression of the Flip-Casp3-GFP reporter. White arrowhead indicates uptake by an epithelial cell. (**c**) An endogenous cell captured during abnormal mitosis (35-38 min), apoptosis (99 min) and its phagocytic uptake (379 min). (**d**) Bax^{+} cells co-expressing Lyn-tdTomato (PM, white arrowheads) expose PS (magenta arrowheads) as detected by injection of AnnexinV-AlexaFluor488 in a live embryo. Yellow arrowheads highlight co-localization of both signals in the same cells. (**e, e´**) *In vivo* detection of Caspase-3 activation by expression of the Flip-Casp3-GFP reporter in Bax^{+} cells co-expressing H2A-mcherry (nucleus). (**e´**) Caspase-3 activation dynamics during nuclear fragmentation. (**f**) Mosaic overexpression of tamoxifen-activated Caspase-8^{ERT2} leads to epithelial uptake (arrowheads) similar to the one observed for Bax^{+} cells. Lyn-tdTomato (plasma membrane (PM) marker, in a-c) and H2a-mCherry (nucleus, in c) were co-expressed in the whole embryo; embryos are Tg(actb1:Lifeact-GFP) in (c), (d) and (f). Scale bars: 20 µm (a,c,e-f), 10 µm (b) and 50 µm (d). Images are representative of most cells observed in 3 (a), 6 (b), 20 (d), and 9 (e,f) embryos and sporadic cell events in 6 (c) embryos.

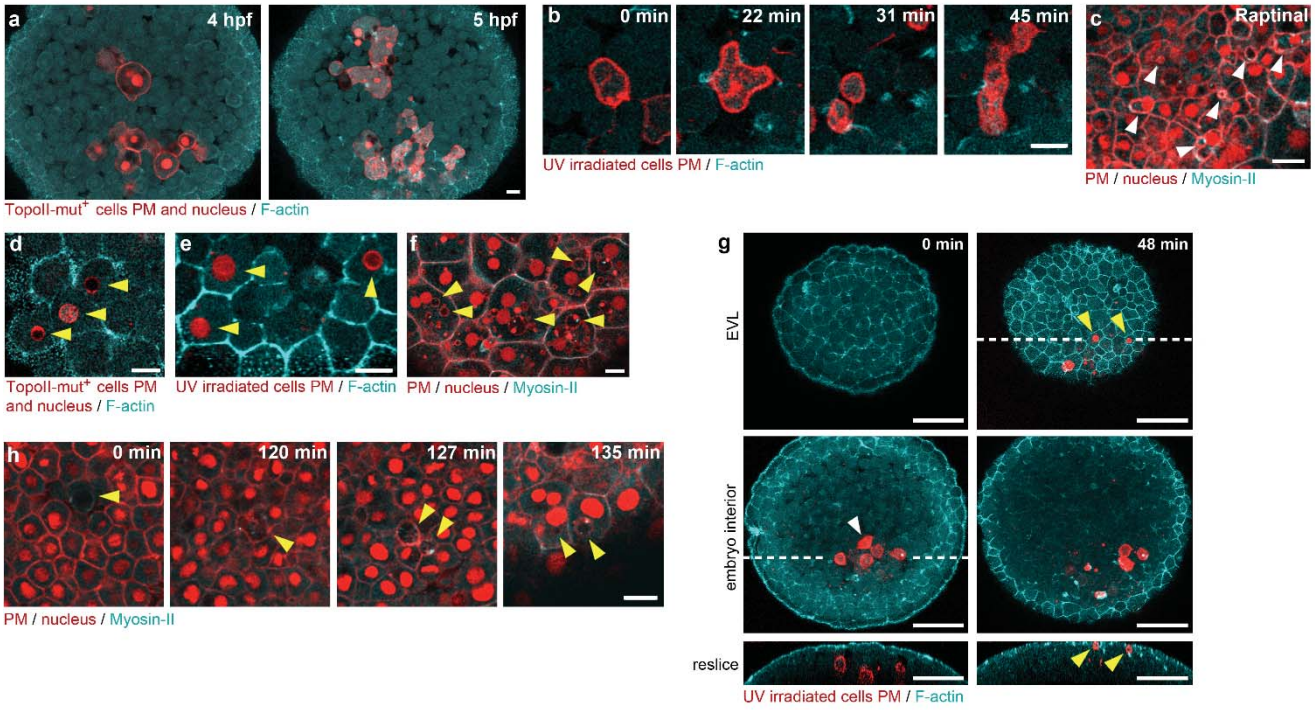

Extended Data Fig. 2. Errors induced by intrinsic or extrinsic stress leads to cell death and epithelial phagocytosis. (**a-g**) Characteristic morphological changes in apoptotic cells (a,b,c white arrowheads) and phagocytic uptake by epithelial cells (d-g, yellow arrowheads) of mutant Topoisomerase II (TopoII-mut) overexpressing cells co-expressing Lyn-TdTomato and H2A-mCherry (a,d), UV-irradiated and transplanted cells expressing Lyn-TdTomato (b,e,g) and cells from Raptinal treated embryos (c,f). In (g), a small number of UV irradiated apoptotic cells were transplanted. White arrowhead indicates a dying cell that is later uptaken by the epithelium as indicated by the yellow arrowheads. Dashed lines indicate the position of the transverse sections. (**h**) Induced programmed cell death by two-photon illumination leading to nuclear fluorescence bleaching (0 min), death (120 min), fragmentation (127 min), and epithelial uptake (135 min) of a single progenitor cell (arrowheads). Embryos are Tg(actb1:Lifeact-GFP) in (a-b,d-e,g) and Tg(Myl12.1-eGFP) in (c), (f) and (h), the latter ones co- expressing Lyn-tdTomato and H2a-mCherry. Scale bars: 20 µm (a-f and h) and 100 µm (g). Images are representative of most cells detected in 6 (a,b,d,e), 8 (c,f) and 3 (d,h) embryos or 5 cells from 5 embryos (g).

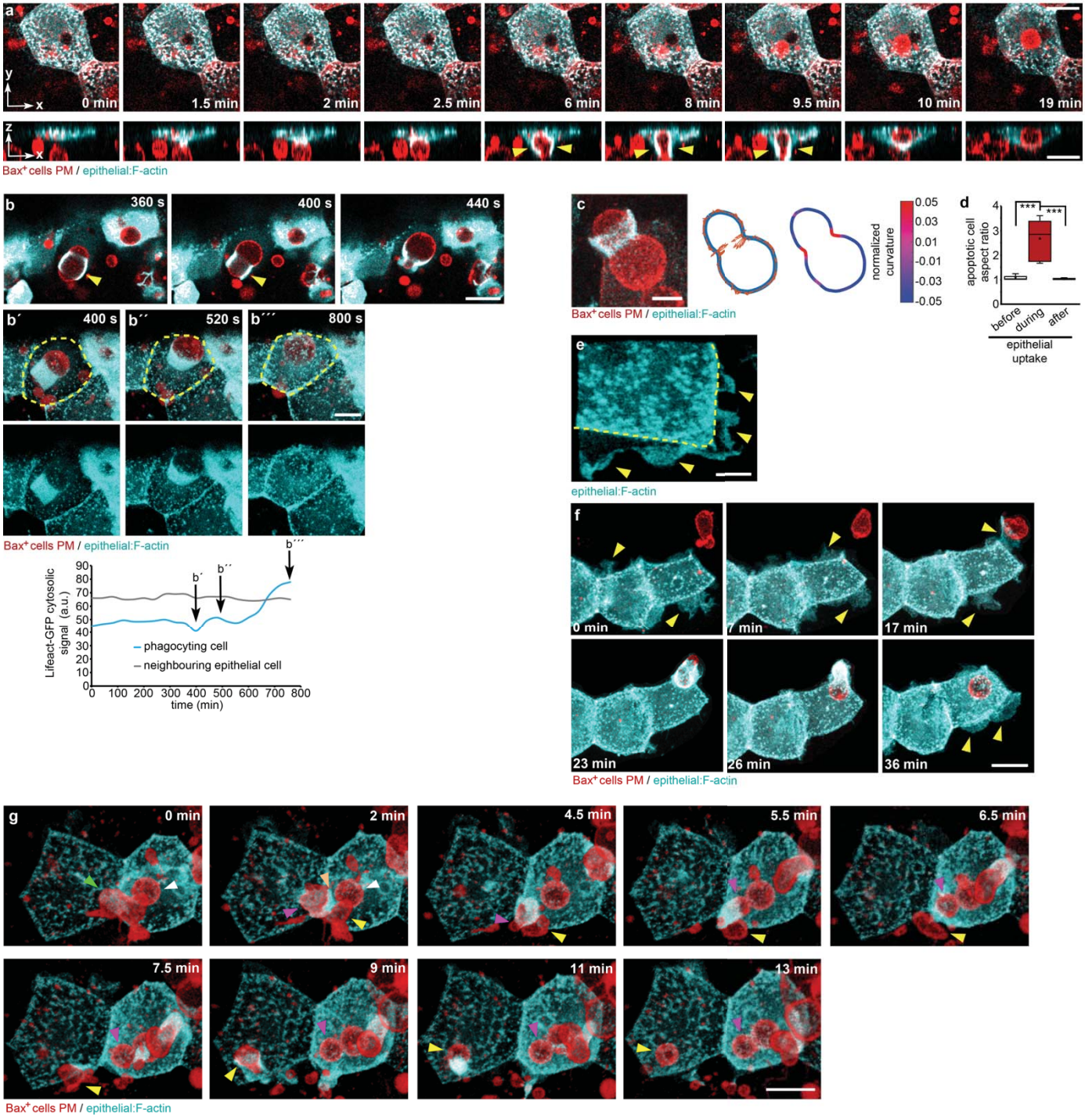

Extended Data Fig. 3. Actin distribution during phagocytic cup formation in epithelial cells. (**a**) A phagocytic event of an apoptotic fragment visualized by slices parallel (top, x-y) and transverse (bottom, x-z) to the surface, in embryos with mosaic Lifeact-GFP staining in single EVL cells. Note the formation of a phagocytic cup by the extension of characteristic actin-rich pseudopods (arrowheads). After engulfment is completed, the z dimension of the epithelial cell remains increased due to the size of the uptaken particle until digestion takes place. (**b,b´**) F-actin accumulates in a phagocytic ring (arrowheads) depleting the cytosolic actin pool (b´). After phagocytosis is completed, actin replenished in the cytosol (b´´´). Quantification of cytosolic actin dynamics is shown on the bottom. Single planes (b) and z-projections (b´-b´´´) are shown. (**c**) Shape deformation of an apoptotic cell during epithelial uptake (left) indicated by curvature vectors normal to the cell perimeter (center) and corresponding scalar bending values (right). (**d**) Aspect ratio of the apoptotic cell before, during, and after uptake (n=6 cells). (**e**) A region of an epithelial cell (dashed line) showing membrane ruffles (arrowheads) with actin accumulations in the front of the ruffles. (**f**) Phagocytic cup formation leading to successful target uptake (23 min-36 min) originating from a membrane ruffle (17 min). Arrowheads indicate

membrane ruffles. (**g**) Collective phagocytosis by different epithelial cells. A single apoptotic cell (green arrowhead) is contacted by an actin protrusion (orange arrowhead) splitting it into two particles (magenta and yellow arrowhead, 2 min). While the left particle (magenta arrowhead) is rapidly phagocytosed by one epithelial cell (from 4.5 min to 7.5 min), the other particle (yellow arrowhead) is only later contacted by another epithelial cell (7.5 min) and then uptaken (from 9 min to 13 min). White arrowhead indicates a previously phagocytosed apoptotic cell. For all panels, Tg(krt18:Gal4FF) embryos were injected with a Tol2-UAS-Lifeact-GFP plasmid. Scale bars: 20 µm (a,b,b′,d) and 5 µm (c,e). Images are representative of most cells detected in 15 (a), 10 (b,c), 20 (e), 20 (g) embryos or some cells in 3 (b′,f) embryos.

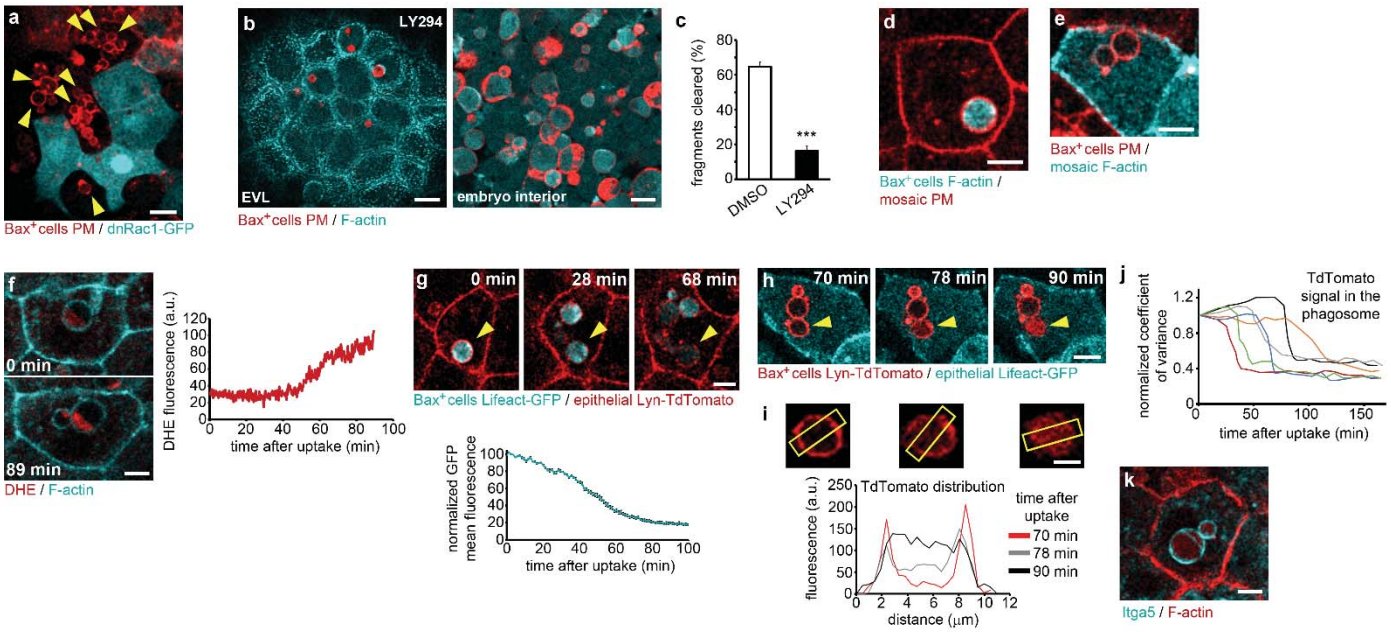

Extended Data Fig. 4. Functional phagosomes are formed upon epithelial phagocytosis. (**a**) Mosaic EVL-specific expression of dnRac1-GFP driven by the krt18 promoter in embryos with mosaic expression of Bax$^+$ cells. dnRac1-GFP epithelial cells do not uptake apoptotic particles, while epithelial neighbors do (arrowheads). (**b,c**) Epithelial phagocytosis of Bax$^+$ cells was evaluated in presence of the PI3K inhibitor LY294 or a DMSO vehicle control (n=8 embryos DMSO; 6 embryos LY294). (**d,e**) Two independent and complementary double mosaic staining allow for identification of the origin of membranes in the phagocytic vesicles. In (d) Bax$^+$ cells express Lifeact-GFP and the epithelial cell expresses Lyn-tdTomato (PM); in (e) Bax$^+$ cells express Lyn-tdTomato (PM) and the epithelial cell expresses Lifeact-GFP. (**f**) Dynamics of superoxide generation in epithelial phagosomes using the DHE reporter. (**g-j**) Degradation of the phagocytic vesicle content using double mosaic staining. Lifeact-GFP (g) or Lyn-TdTomato (h-j) fluorescence coming only from the apoptotic cell (Lyn-TdTomato (g) or Lifeact-GFP (h) were expressed in epithelial cells) was monitored after phagocytosis. (g) GFP fluorescence decrease (n=7 phagosomes), known to be associated to both pH-dependent quenching and protein degradation[1,2]. (h-i) Change in spatial distribution of Lyn-TdTomato fluorescence, indicative of a lytic activity degrading (or releasing the protein from) the plasma membrane of the ingested apoptotic cell (DsRed derived fluorescent proteins are resistant to degradation by lysosomal enzymes[1]). (j) Dynamic quantification of the variance of the Td-Tomato signal in the whole phagosome (each line corresponds to a single phagosome). Redistribution begins 55.3 +/- 9.5 min after internalization and takes 24.8 +/- 3.4 min to be completed. (**h**) The Itga5-GFP protein decorates epithelial phagosomes. Embryos are Tg(Krt18:Gal4FF) injected with a Tol2-UAS-dnRac1-GFP plasmid in (a), Tg(actb1:Lifeact-GFP) in (b,f) and Tg(actb1:Lifeact-RFP) in (k). Scale bars: 20 µm (a,b), 10 µm (d,g,h,k) and 5 µm (i). Images are representative of 6 (a) embryos, or most cells detected from 3 (d,e,f) and 6 (k) embryos. Mean and standard error are shown. *** $p<0.0001$.

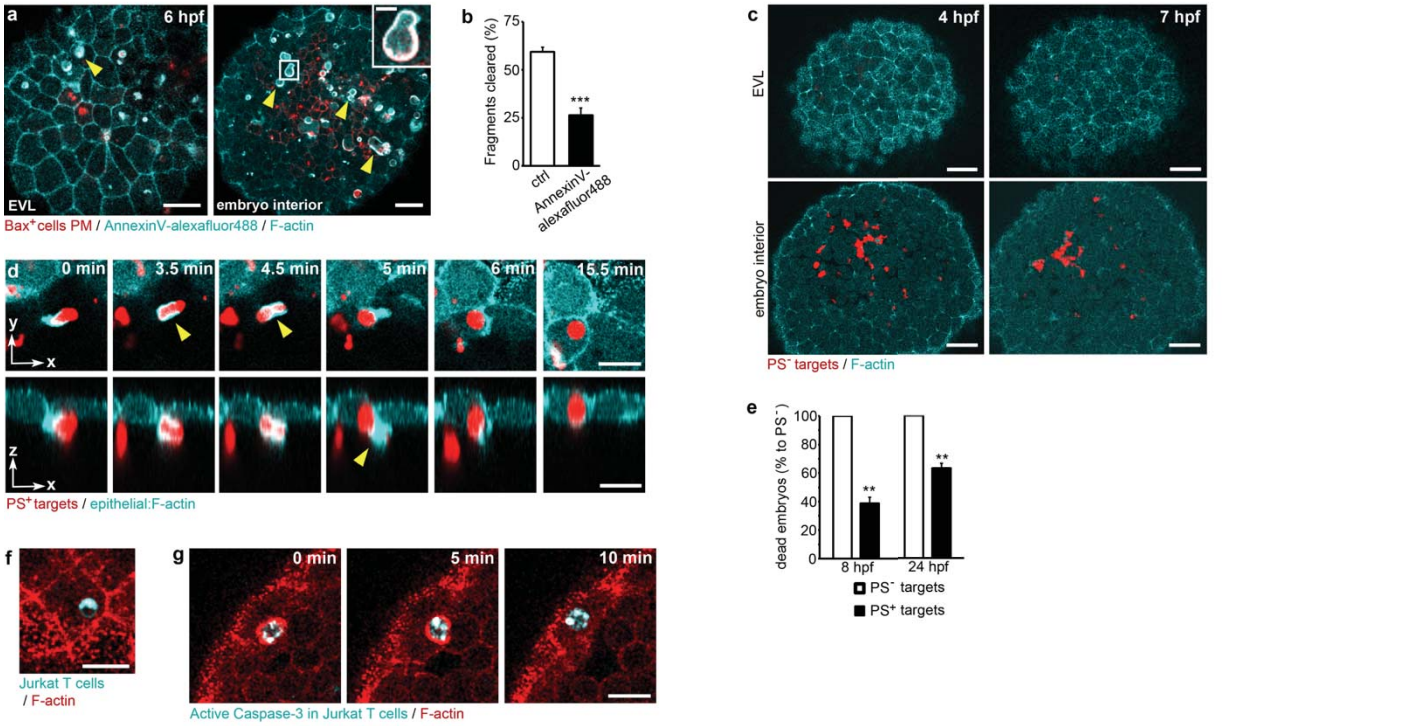
a
6 hpf
EVL
embryo interior
Bax+cells PM / AnnexinV-alexafluor488 / F-actin
b
Fragments cleared (%)
75
50
25
0
***
ctrl
AnnexinV-alexafluor488
c
4 hpf
7 hpf
EVL
embryo interior
PS- targets / F-actin
d
0 min
3.5 min
4.5 min
5 min
6 min
15.5 min
y
x
z
x
PS+ targets / epithelial:F-actin
e
dead embryos (% to PS-)
100
80
60
40
20
0
**
**
8 hpf
24 hpf
PS- targets
PS+ targets
f
Jurkat T cells
/ F-actin
g
0 min
5 min
10 min
Active Caspase-3 in Jurkat T cells / F-actin

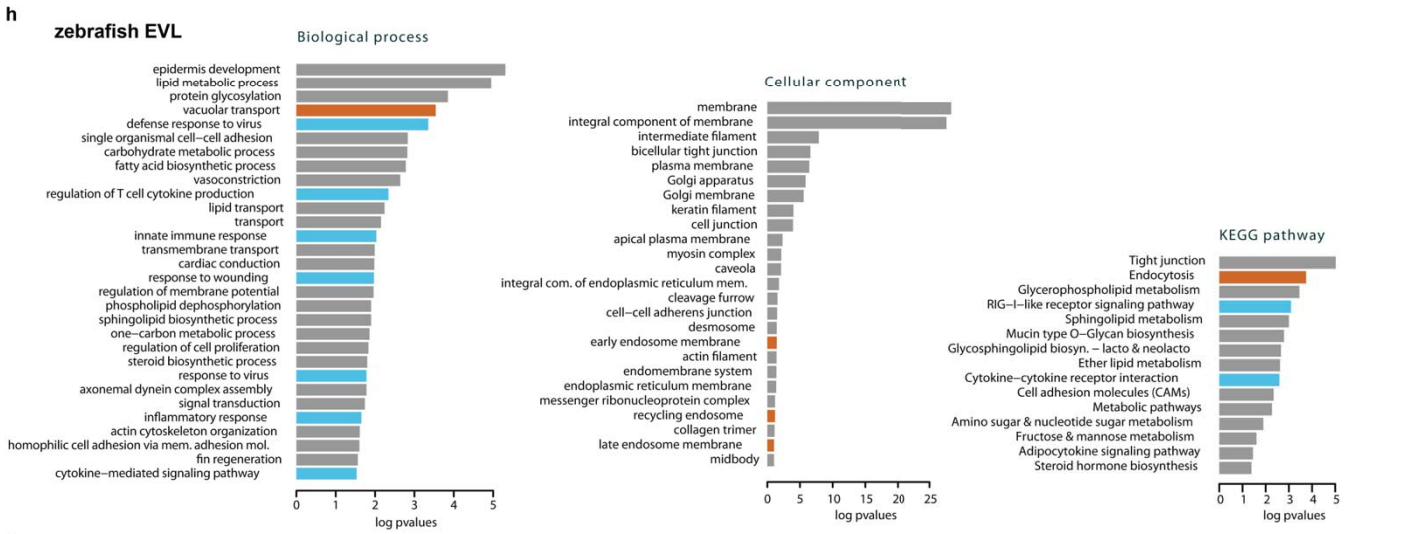
h
zebrafish EVL
Biological process
epidermis development
lipid metabolic process
protein glycosylation
vacuolar transport
defense response to virus
single organismal cell–cell adhesion
carbohydrate metabolic process
fatty acid biosynthetic process
vasoconstriction
regulation of T cell cytokine production
lipid transport
transport
innate immune response
transmembrane transport
cardiac conduction
response to wounding
regulation of membrane potential
phospholipid dephosphorylation
sphingolipid biosynthetic process
one–carbon metabolic process
regulation of cell proliferation
steroid biosynthetic process
response to virus
axonemal dynein complex assembly
signal transduction
inflammatory response
actin cytoskeleton organization
homophilic cell adhesion via mem. adhesion mol.
fin regeneration
cytokine–mediated signaling pathway
0 1 2 3 4 5
log pvalues
Cellular component
membrane
integral component of membrane
intermediate filament
bicellular tight junction
plasma membrane
Golgi apparatus
Golgi membrane
keratin filament
cell junction
apical plasma membrane
myosin complex
caveola
integral com. of endoplasmic reticulum mem.
cleavage furrow
cell–cell adherens junction
desmosome
early endosome membrane
actin filament
endomembrane system
endoplasmic reticulum membrane
messenger ribonucleoprotein complex
recycling endosome
collagen trimer
late endosome membrane
midbody
0 5 10 15 20 25
log pvalues
KEGG pathway
Tight junction
Endocytosis
Glycerophospholipid metabolism
RIG–I–like receptor signaling pathway
Sphingolipid metabolism
Mucin type O–Glycan biosynthesis
Glycosphingolipid biosyn. – lacto & neolacto
Ether lipid metabolism
Cytokine–cytokine receptor interaction
Cell adhesion molecules (CAMs)
Metabolic pathways
Amino sugar & nucleotide sugar metabolism
Fructose & mannose metabolism
Adipocytokine signaling pathway
Steroid hormone biosynthesis
0 1 2 3 4 5
log pvalues

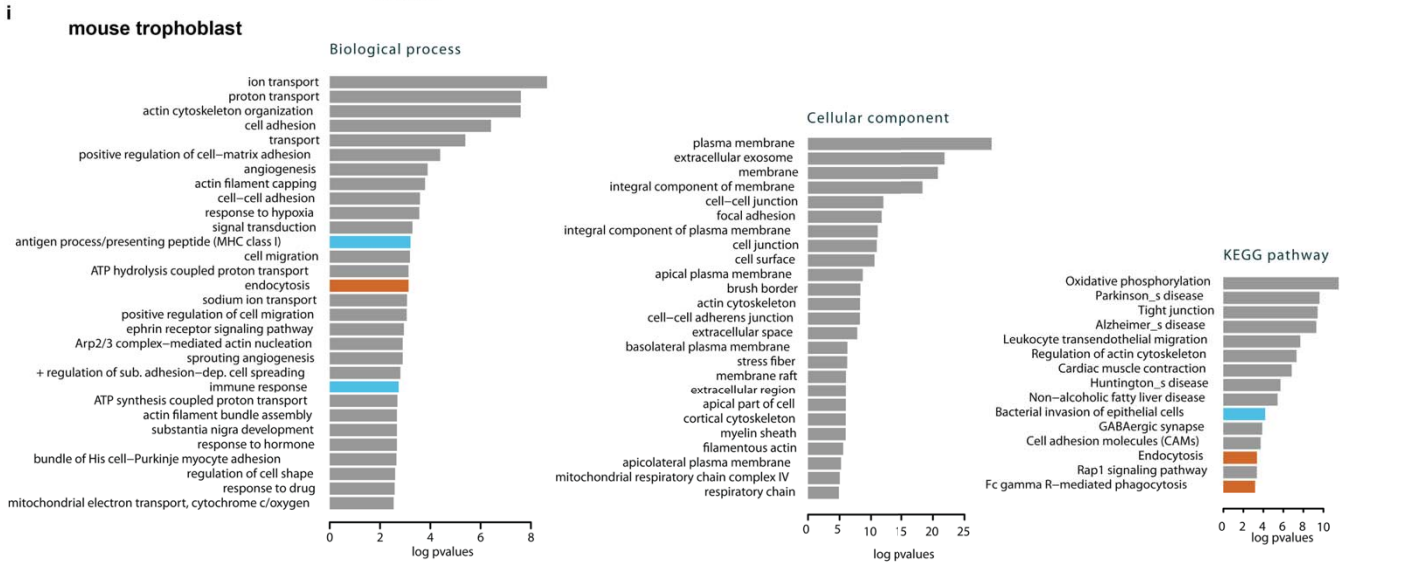
i
mouse trophoblast
Biological process
ion transport
proton transport
actin cytoskeleton organization
cell adhesion
transport
positive regulation of cell–matrix adhesion
angiogenesis
actin filament capping
cell–cell adhesion
response to hypoxia
signal transduction
antigen process/presenting peptide (MHC class I)
cell migration
ATP hydrolysis coupled proton transport
endocytosis
sodium ion transport
positive regulation of cell migration
ephrin receptor signaling pathway
Arp2/3 complex–mediated actin nucleation
sprouting angiogenesis
+ regulation of sub. adhesion–dep. cell spreading
immune response
ATP synthesis coupled proton transport
actin filament bundle assembly
substantia nigra development
response to hormone
bundle of His cell–Purkinje myocyte adhesion
regulation of cell shape
response to drug
mitochondrial electron transport, cytochrome c/oxygen
0 2 4 6 8
log pvalues
Cellular component
plasma membrane
extracellular exosome
membrane
integral component of membrane
cell–cell junction
focal adhesion
integral component of plasma membrane
cell junction
cell surface
apical plasma membrane
brush border
actin cytoskeleton
cell–cell adherens junction
extracellular space
basolateral plasma membrane
stress fiber
membrane raft
extracellular region
apical part of cell
cortical cytoskeleton
myelin sheath
filamentous actin
apicolateral plasma membrane
mitochondrial respiratory chain complex IV
respiratory chain
0 5 10 15 20 25
log pvalues
KEGG pathway
Oxidative phosphorylation
Parkinson_s disease
Tight junction
Alzheimer_s disease
Leukocyte transendothelial migration
Regulation of actin cytoskeleton
Cardiac muscle contraction
Huntington_s disease
Non–alcoholic fatty liver disease
Bacterial invasion of epithelial cells
GABAergic synapse
Cell adhesion molecules (CAMs)
Endocytosis
Rap1 signaling pathway
Fc gamma R–mediated phagocytosis
0 2 4 6 8 10
log pvalues

Extended Data Fig. 5. Molecular pathways involved in epithelial phagocytosis. (**a,b**) Epithelial clearance in AnnexinV-AlexaFluor488 injected embryos. Arrowheads indicate Bax^+ cell fragments co-labelled with Lyn-tdTomato (PM) and AnnexinV-AlexaFluor488 (overlay in white) at 6 hpf (n=8 embryos). (**c**) Surrogate targets not containing PS (PS^-, formed by lipid aggregates of PC and TexasRed-DHPE) injected in the blastula embryo are not cleared. (**d**) Dynamics of a single phagocytic event of a PS^+ target (lipid aggregate containing PS, PC and TexasRed-DHPE). Note the formation of the actin ring in the phagocytic cup (3.5 min and 4.5 min) and actin accumulation at the rear (5 min) during particle uptake (arrowheads). Slices parallel (top, x-y) and transverse (bottom, x-z) to the surface are shown. (**e**) Death rate of embryos injected at 4 hpf with a large number of surrogate targets (3 independent experiments with n>70 embryos per condition). (**f,g**) Epithelial phagocytosis of apoptotic UV-irradiated human Jurkat T cells transplanted into a zebrafish embryo. Membrane (f) and Caspase-3 chemical reporter (g) staining of transplanted apoptotic Jurkat T cells. (**h,i**) Top enriched gene ontology terms for Zebrafish EVL cells versus progenitor cells (h, 3 independent replicates, about 1000 embryos per sample) and Mouse TE cells versus ICM (i), showing raw p values for biological process (left), cellular component (middle) and KEGG pathway (right). Results were made using DAVID and a background of genes that were expressed above baseMean 3 (from DESeq2). Blue bar represent immune related functions and orange bars phagocytosis related terms. Embryos are Tg(actb1:Lifeact-GFP) in (a,c), Tg(krt18:Gal4FF/UAS:Lifeact-GFP) in (d), Tg(actb1:Lifeact-RFP) in (f-g). Scale bars: 50 µm (a,c), 10 µm (a inset) and 20 µm (d,f,g). Mean and standard error are shown. *** $p<0.0001$, ** $p<0.005$. Images are representative of 5 (c) embryos, most cells detected from 7 (f) and 2 (g) embryos, or some targets detected from 6 embryos (d).

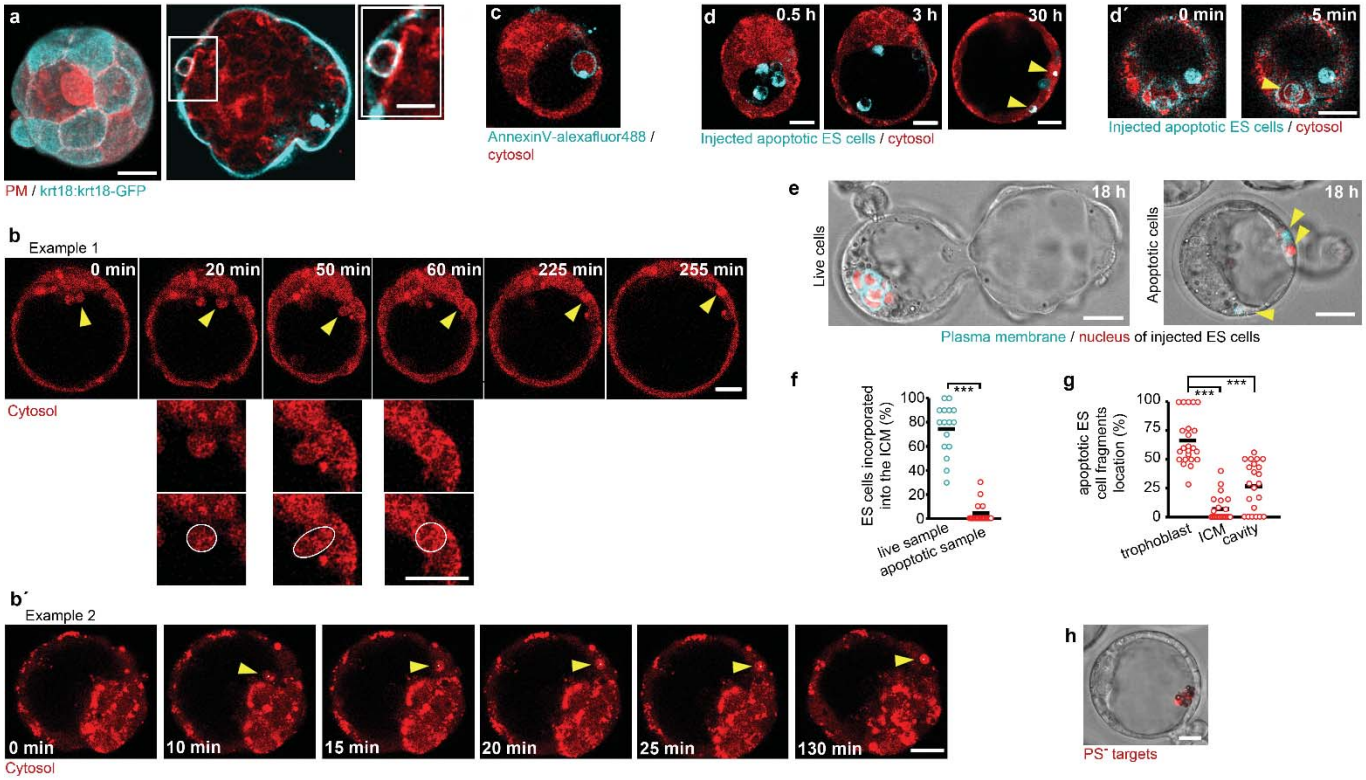

Extended Data Fig. 6. Epithelial phagocytosis of apoptotic targets in zebrafish embryoids and conservation in mouse embryos. (**a**) Self-organizing blastula cell aggregates recapitulate de novo formation of a surface phagocytic epithelium (maximum z-projection on the left and single slice on the right), showing krt18 promoter activity, squamous epithelial morphology and junction formation in their surface cells, and their ability to engulf particles (inset). Cells for embryoid generation were obtained from Tg(krt18:krt18-GFP) embryos co-expressing Lyn-tdTomato (PM). (**b,b´**) Time-lapse imaging of DsRed-expressing blastocysts. (b) A cell from the inner cell mass (dotted line) is released to the cavity (0 min), phagocytosed (50 and 60 min) and remains inside the trophoblast cell during blastocyst expansion (255 min). Note the deformation of the particle during uptake similar to the one occurring during phagocytosis in the zebrafish epithelium (insets). (b´) A second example of the same process described in (b). (**c**) Injection of AnnexinV-AlexaFluor488 into the cavity of unperturbed live blastocysts. (**d**) Dynamics of apoptotic mouse ES cells injected into the blastocyst cavity and their localization inside trophoblast cells (arrowheads) 30 hours after injection. A detailed view of the uptake process is shown on the right (d'): an ES cell appears inside an epithelial cell (arrowhead), similar to epithelial uptake in zebrafish embryos. (**e-g**) Representative images (e) and quantitative analysis (f-g) of the final localization of live or apoptotic mouse ES cells injected into the blastocyst cavity. (f) Most live mES cells were incorporated into the ICM (n=16 embryos). (g) Apoptotic mES fragments were mainly found inside the trophoblast (yellow arrowheads in (e), n=23 embryos). mES cells express GPI-GFP (plasma membrane) and H2B-mCherry (nucleus). (**h**) PS^- surrogate targets (glass spheres coated with PC and TexasRed-DHPE) are not uptaken by the trophoblast and remain in the blastocyst cavity. *** p>0.0001. Scale bars: 25 µm (a), 10 µm (a inset), 20 µm (b,b´,c,d,d´) and 30 µm (e). Images are representative of 21 aggregates (a, 3 independent assays), 10 (d) and 6 (h) embryos, or some cells detected from 4 (b,b´) and 3 (c) embryos.

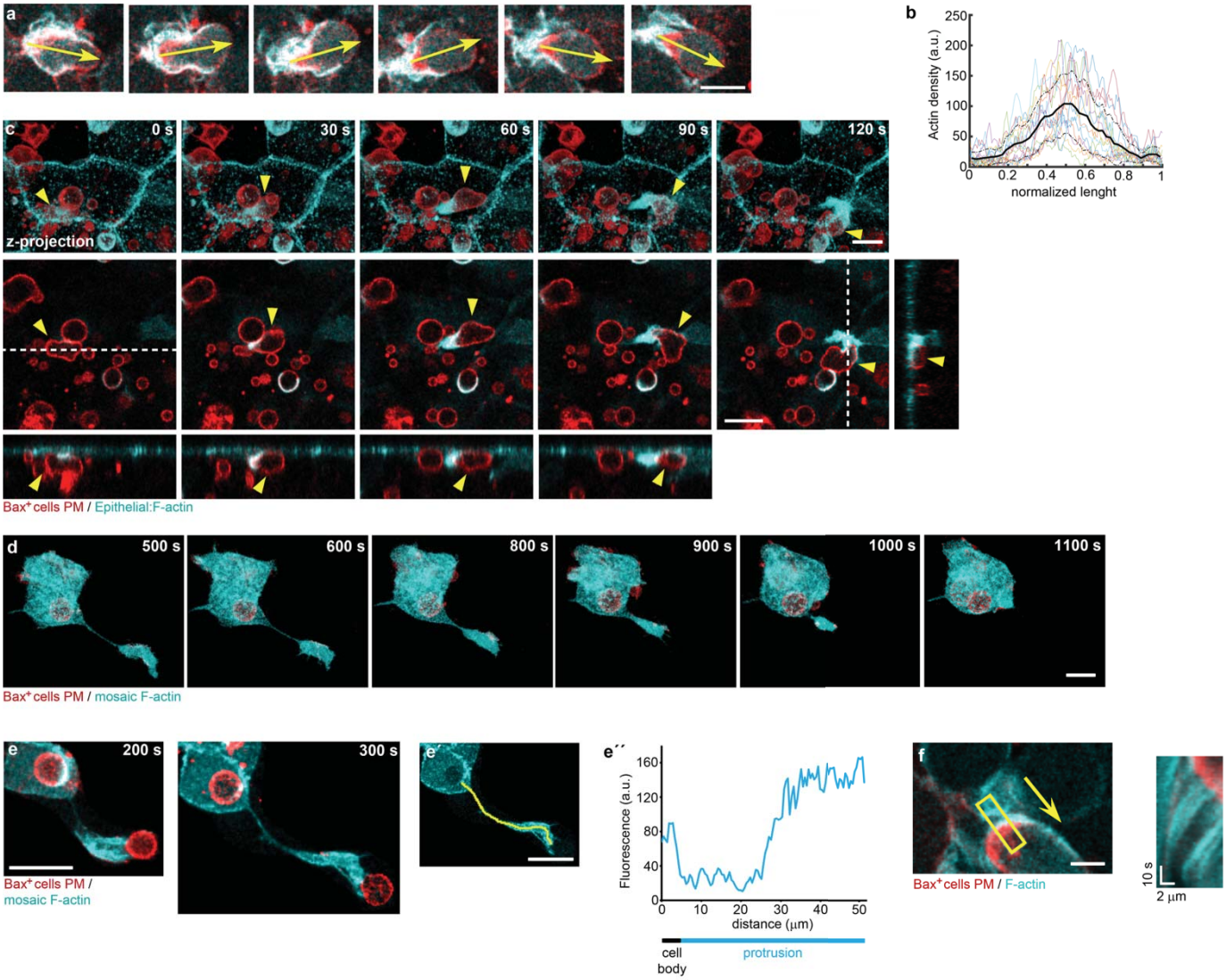

Extended Data Fig. 7. F-actin dynamics in epithelial arm protrusions. (**a,b**) External F-actin localizes to the rear part of the apoptotic cell. Arrowheads represent the direction of movement (a). External F-actin distribution along the normalized apoptotic cell perimeter (b, x=0.5 corresponds to the rear of the apoptotic cell, n=15 cells). (**c**) Lifeact-GFP expression driven by the krt18 promoter to visualize F-actin specifically in the epithelial tissue. Z-projection (top), single slice z-section (middle), and transverse sections at the location of the dashed lines (bottom and lateral) are shown. An apoptotic particle (arrowheads) starts to move in close association with epithelial actin enrichment. (**d**) Epithelial arm protrusions retract after extension, related to Fig. 2i. (**e**) F-actin enrichment is located at the tip of the epithelial protrusion, where the protrusion contacts the apoptotic cell. (e´,e´´) Quantification of Lifeact-GFP fluorescence levels over the yellow line. (**f**) F-actin flow in the external actin accumulation at the apoptotic cell rear. The kymograph (right) was created from the yellow box in the left. The yellow arrow indicates the direction of movement of the apoptotic particle. Embryos are Tg(actb1:Lifeact-GFP) in (a) and (f), Tg(krt18:Gal4FF/UAS:Lifeact-GFP) in (c). Lifeact-GFP is expressed mosaically in (d) and (e). Scale bars: 20 µm (a,c,d,e,e´) and 5 µm (f). Images are representative of most cells from 20 (a), 9 (c) and 7 (d,e) embryos or some cells detected from 3 (f) embryos.

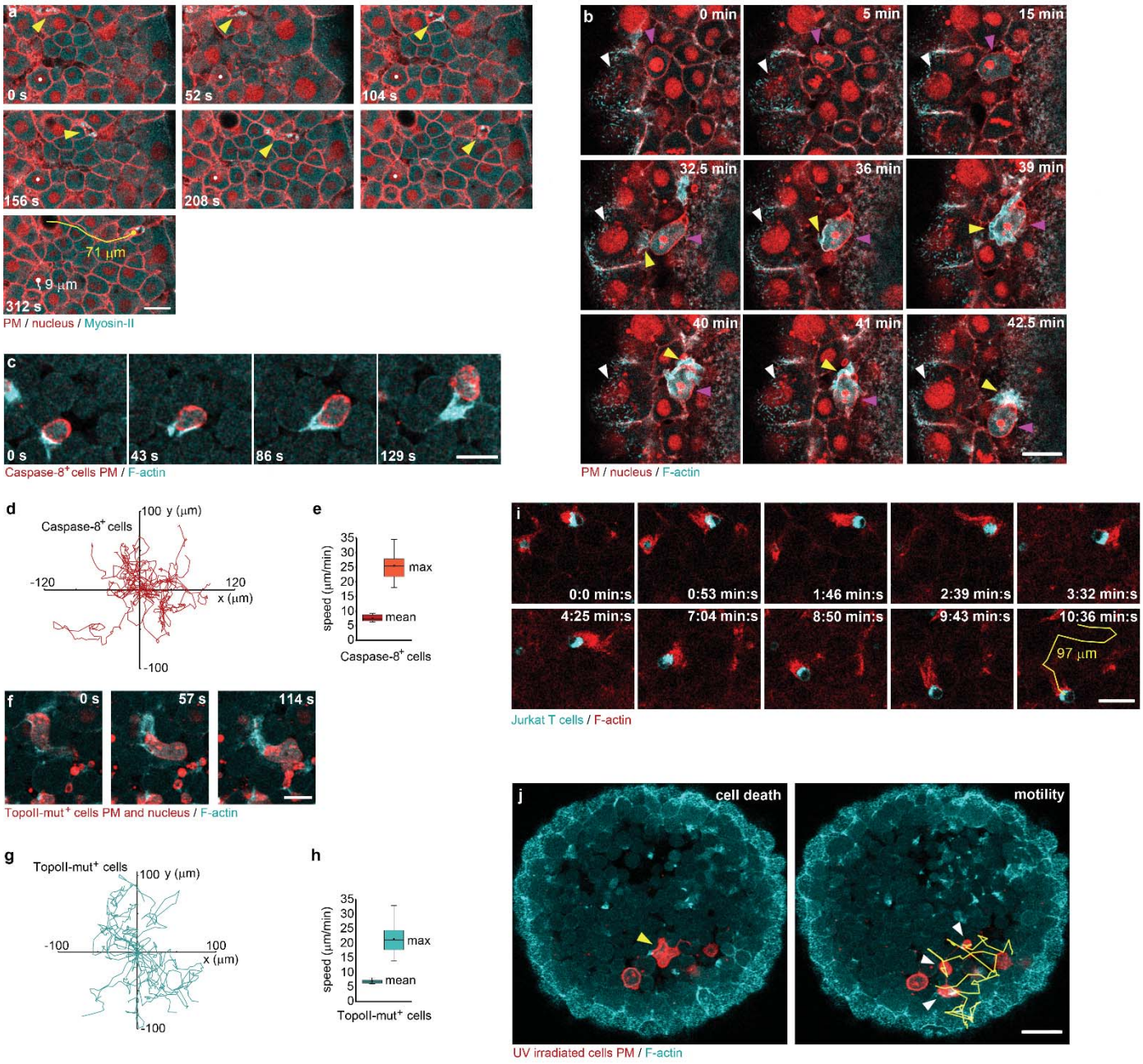

Extended Data Fig. 8. Apoptotic motility and epithelial arms are present in various apoptotic contexts. (**a**) Endogenous apoptotic fragment (arrowhead) revealing fast motility (yellow line indicates the total apoptotic path length). The path of a live cell (white dots and line) is shown as a comparison. (**b**) Epithelial arm formation in contact with an endogenous apoptotic cell. F-actin (yellow arrowheads) accumulates in an epithelial cell (white arrowheads) in contact with an apoptotic cell (magenta arrowhead), after its nuclear fragmentation. 10 min after the initial contact (32.5 min), external actin polarizes to the rear of the motile apoptotic cell (yellow arrowheads). (**c-h**) Motility of Caspase-8^{ERT2} (c-e) or TopoII-mut (f-h) apoptotic cells. Representative images of association with actin-rich arms (c,f), x-y trajectories (d,g), and speed (e,h; Caspase-8^+ cells $<v_{mean}>$= 7.5 +/- 0.3 µm/min, $<v_{max}>$= 25.5 +/- 1.1 µm/min, n=17 cells from 3 embryos; TopoII-mut cells $<v_{mean}>$= 6.8 +/- 0.1 µm/min, $<v_{max}>$= 21.3 +/- 1.3 µm/min, n=17 cells from 4 embryos) of apoptotic cells. (**i**) Motility and association with epithelial arms of UV-irradiated human Jurkat T cells. (j) Cell death (yellow arrowhead) followed by fragmentation (white arrowheads) and motility (yellow tracks) of few UV-irradiated and transplanted cells expressing Lyn-TdTomato. Embryos are Tg(actb1:Myl12.1-eGFP) in (a), Tg(actb1:Lifeact-GFP) in (b,c,f,j), and Tg(actb1:Lifeact-RFP) in (i); In (a,b,f) embryos (a,b) or TopoII-mut cells (f) co-express Lyn-tdTomato (PM) and H2a-mCherry (nucleus); In (c) Caspase-8 co-express Lyn-tdTomato (PM); In (i) membranes of Jurkat cells were stained with BODIPY-FL-C5-Ceramide before transplantation. Scale bars: 20 µm (a,b,c,i), 10 µm (f), and 50 µm (j). Images are representative of some cells from 7 (a) and 4 (b) embryos, or most cells from 3 (i,j) embryos.

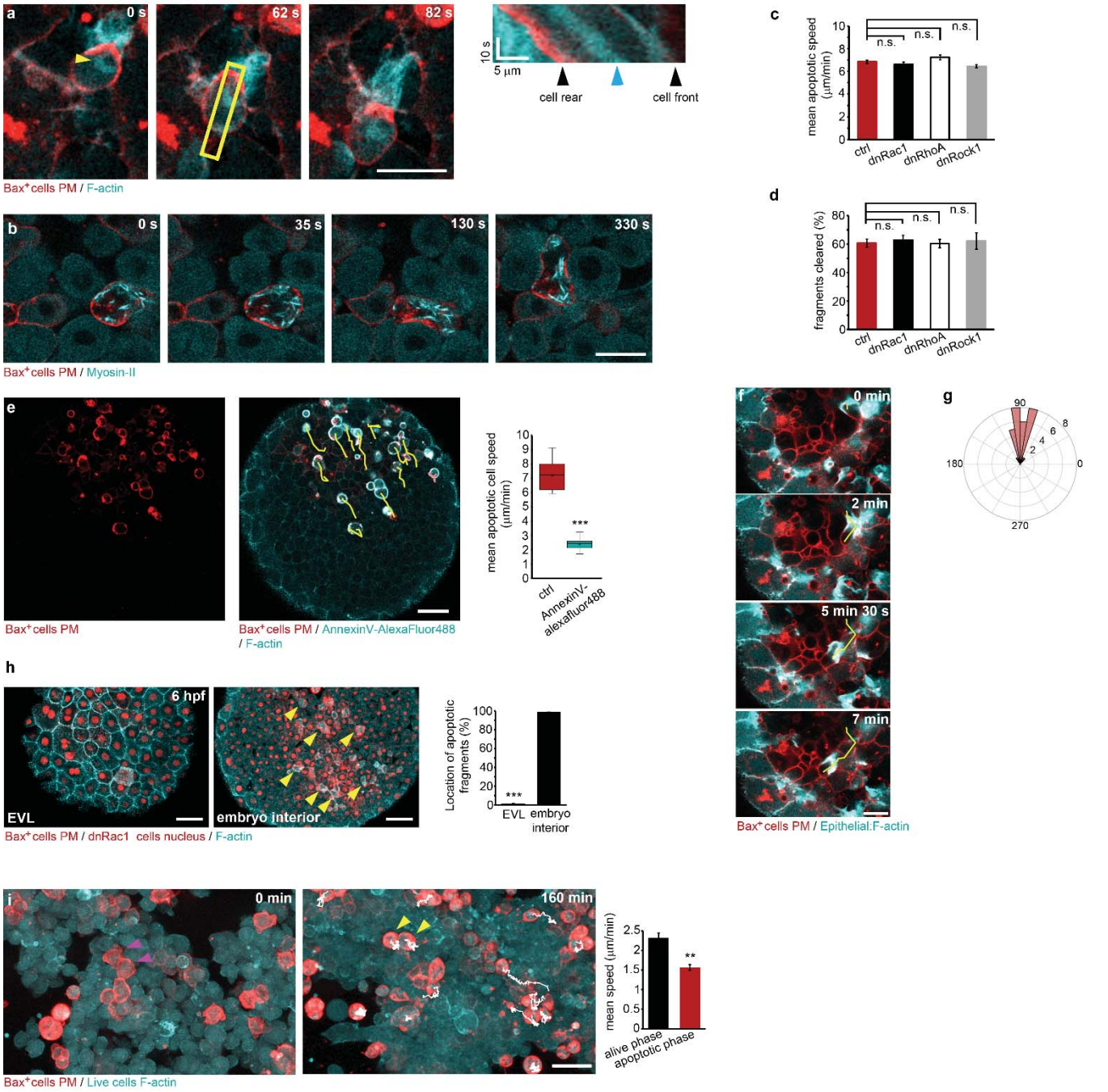

Extended Data Fig. 9. Possible factors underlying apoptotic motility. (**a,b**) *In vivo* high-speed single cell imaging of F-actin and Myosin II dynamics in motile apoptotic cells. (a) Apoptotic cell internal F-actin distribution (arrowhead) is static during cell movement (see kymograph on the right generated from the yellow box region; blue arrowhead highlights the passive movement of actin together with the cell front and rear. (**b**) Accumulation of Myosin II in static rods is shown. (**c,d**) Analysis of apoptotic cell speed (c) and phagocytic uptake (d) in Bax$^+$ cells co-expressing the indicated dominant negative proteins (c: n=28 control cells, 16 dnRac1 cells, 40 dnRhoA cells and 26 dnRock1 cells; d: n=11 control embryos, 11 embryos with dnRac1 cells, 9 embryos with dnRhoA cells, 9 embryos with dnRock1 cells). (**e**) Apoptotic cell motility in AnnexinV injected embryos. Bax$^+$ cells co-expressing Lyn-tdTomato (PM) (left) and co-labelled with AnnexinV-AlexaFluor488 (center, overlay in white) are shown. Yellow paths correspond to a period of 30 min of tracking. Mean instantaneous speed are also shown on the right (n=15 cells from 3 control embryos; n=20 cells from 5 AnnexinV injected embryos). (f) Actin arms associated to apoptotic motility in embryos with Lifeact-GFP expressed specifically in the EVL tissue. (g) Angular histogram of apoptotic particle movement direction (tlag=60 s) measured as the angular difference relative to the peak of F-actin density localization from epithelial arm protrusions (oriented to -270°, n=15 cells, 6 embryos). The histogram indicates that whenever an apoptotic particle

undergoes directional movement the actual F-actin accumulation (EVL specific labelling) is centered at the back of the apoptotic fragment. (h) Analysis of epithelial phagocytic uptake in conditions of whole embryo dnRac1 expression (n=4 embryos). Arrowheads indicate apoptotic cells. (i) Motility analysis of a co-culture of apoptotic (Bax^{+}) and live cells in vitro. The red cells were tracked before (magenta arrowheads) and after apoptosis (yellow arrowheads). White lines show examples of apoptotic tracks (n=14 cells from 3 experiments). Embryos (and cells obtained thereof) are Tg(actb1:Lifeact-GFP) in (a,e,h-i), Tg(Myl12.1-eGFP) in (b) and Tg(krt18:Gal4FF/UAS:Lifeact-GFP) in (f). Scale bars: 20 μm (a,b,f) and 50 μm (e,h-i). Mean and standard error are shown. *** $p>0.0001$, ** $p<0.005$. Images are representative of most cells from 10 (a), 5 (b) and 6 (h) embryos.

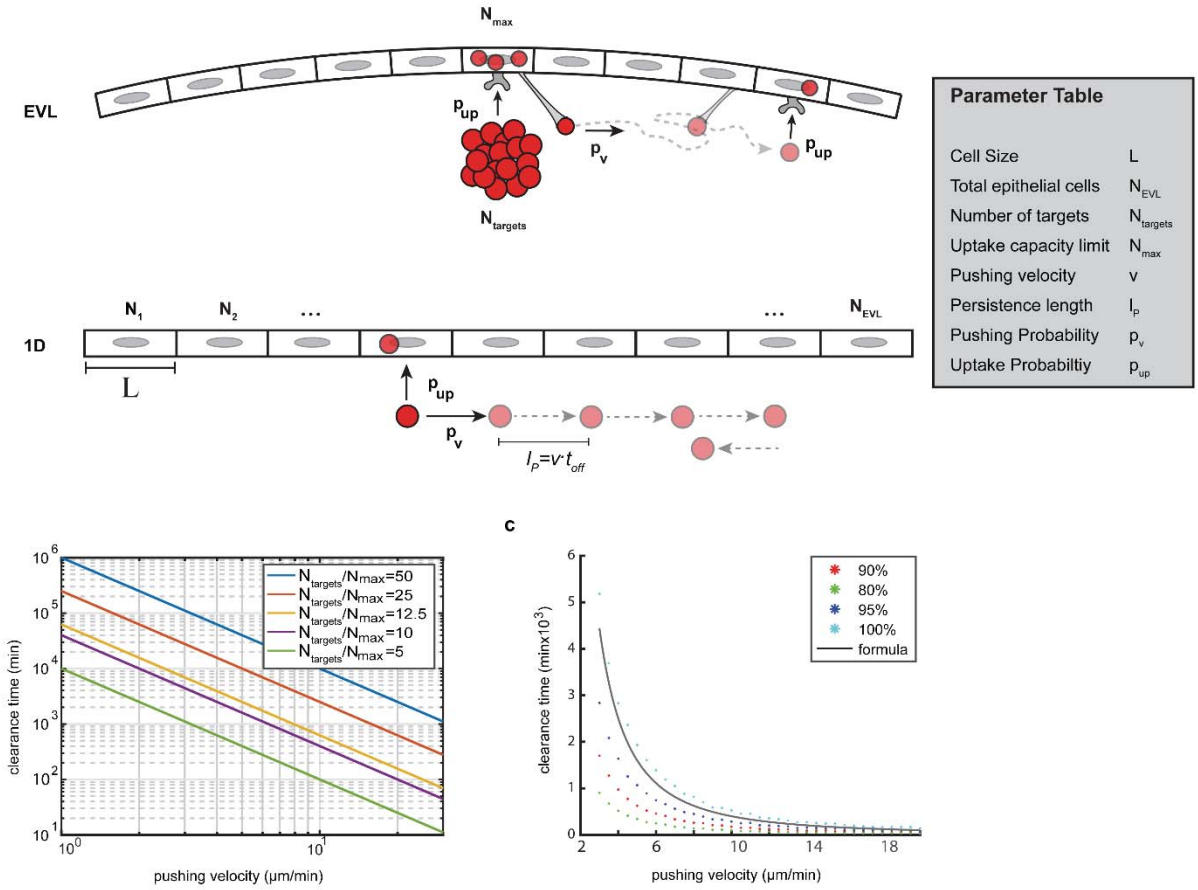

Extended Data Fig. 10. (**a**) Schematic illustration of experimental condition (top) showing a local source of apoptotic targets (red) underneath an epithelial layer (EVL). Individual epithelial cells can form two types of basal protrusions, phagocytic cups (formed at a rate p_{up}), which mediate target ingestion, and epithelial arms (formed at a rate p_v), which actively push apoptotic targets with velocity v and induce target dispersal underneath the epithelial layer. Each epithelial cell can engulf a maximum number of targets N_{max}. Schematic of the 1D Monte Carlo simulation (bottom), and the minimal set of parameters included therein (right). (**b**) Clearance time as a function of pushing speed v for various values of N_{target}/N_{max}. The clearance time decreases with $\sim v^2$ and $\sim (N_{target}/N_{max})^2$. (**c**) Tissue clearance time as a function of pushing speed v for various clearance efficiencies. The analytically derived clearance time matches the clearance time from Monte Carlo simulations at approximately 98% clearance efficiency.

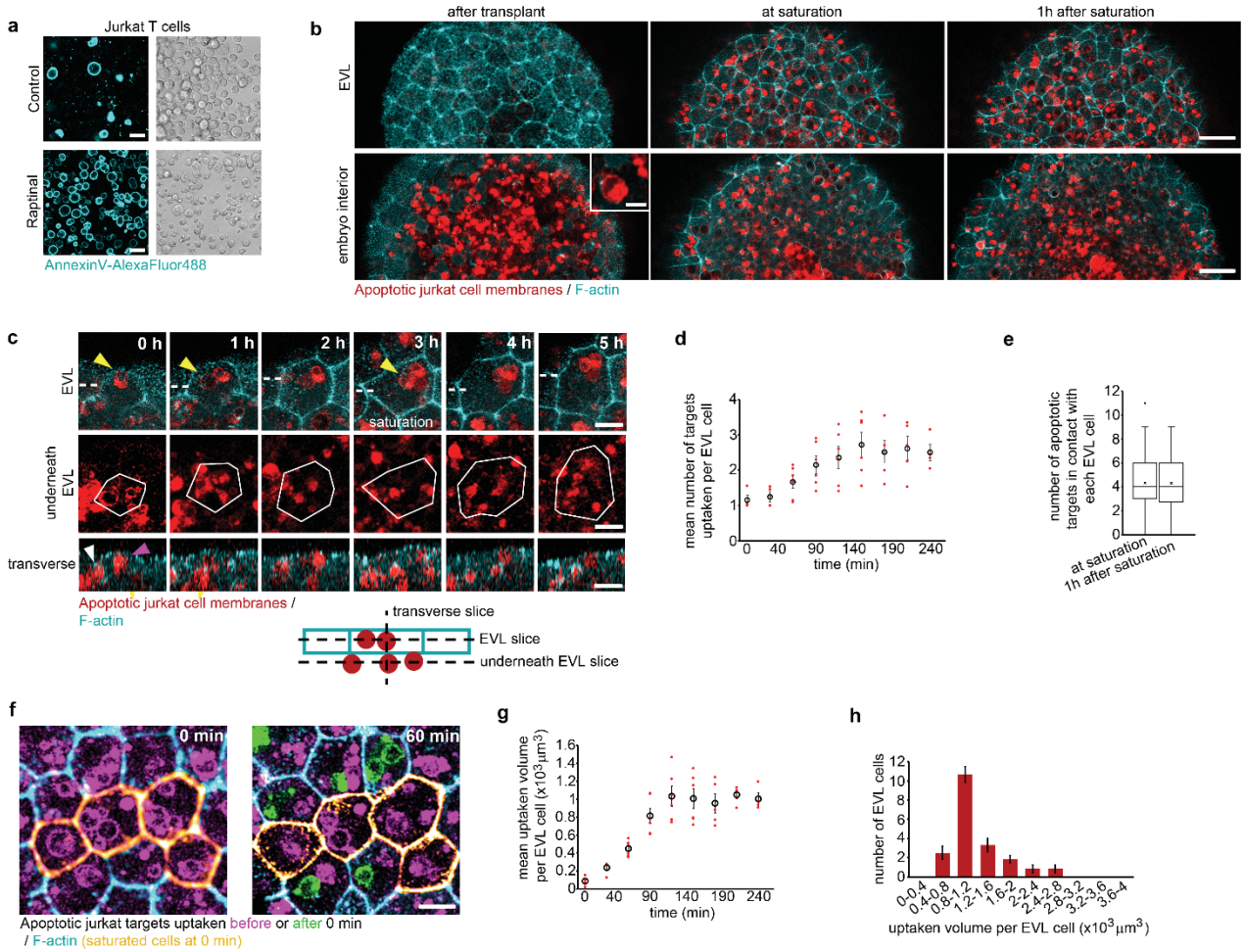

Extended Data Fig. 11. *In vivo* analysis of epithelial uptake efficiency. (**a**) AnnexinV-AlexaFluor488 staining of Raptinal-treated (or control) Jurkat cells before transplantation (% of Annexin$^+$ cells: 97.4+/-0.4 for Raptinal, 10.3+/-0.8 for control; n=3 independent experiments, 90-120 cells per sample). (**b**) Interior of the embryo and EVL surface uptake after transplantation of apoptotic Jurkat cells (left), at the moment of reaching saturation (center) and 1 h after saturation (right). Inset highlights the morphology of a non-fragmented Jurkat cell. (**c**) Detail of an EVL cell sequentially uptaking 3 apoptotic targets (yellow arrowheads indicate a new particle detected inside the cell). In the transverse section, the presence of uptaken (magenta arrowhead) and non-uptaken (white arrowhead) targets is highlighted. The section underneath the EVL shows multiple non-uptaken targets in contact with the saturated cell (white polygon). (**d**) Mean number of apoptotic targets uptaken per EVL cell over time (n= 120 cells from 6 embryos). (**e**) Quantification of the external non-uptaken apoptotic targets contacted by single EVL cells at or 1h after saturation (n= 69 (at saturation) and 58 (1 h after saturation) cells from 6 embryos). (**f**) Neighboring epithelial cells (cyan) to a region of saturated cells (orange) are still able to uptake apoptotic targets (green). (**g**) Mean volume of apoptotic targets uptaken per EVL cell over time (n= 120 cells from 6 embryos). (**h**) Distribution of volume uptaken by EVL cells at saturation (n=6 embryos). In (b,c,f) Jurkat cells are stained with FM™ 4-64FX and embryos are Tg(actb1:Lifeact-GFP). Scale bars: 20 µm (a,c,h), 50 µm (b) and 5 µm (b inset).

Extended data table

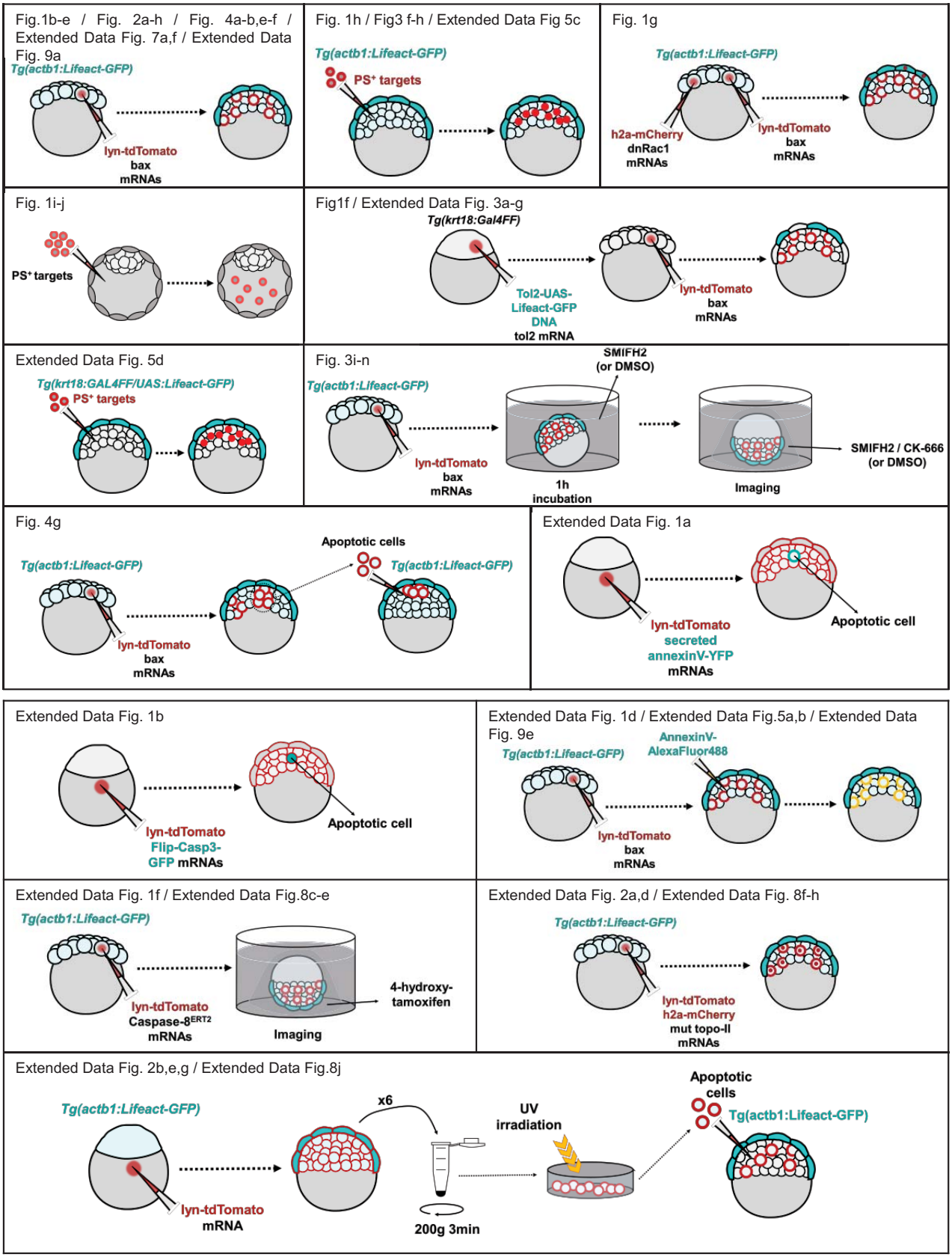

Extended data Table. Part 1. Schemes of the experiments performed detailing the staining and the corresponding figure panel.

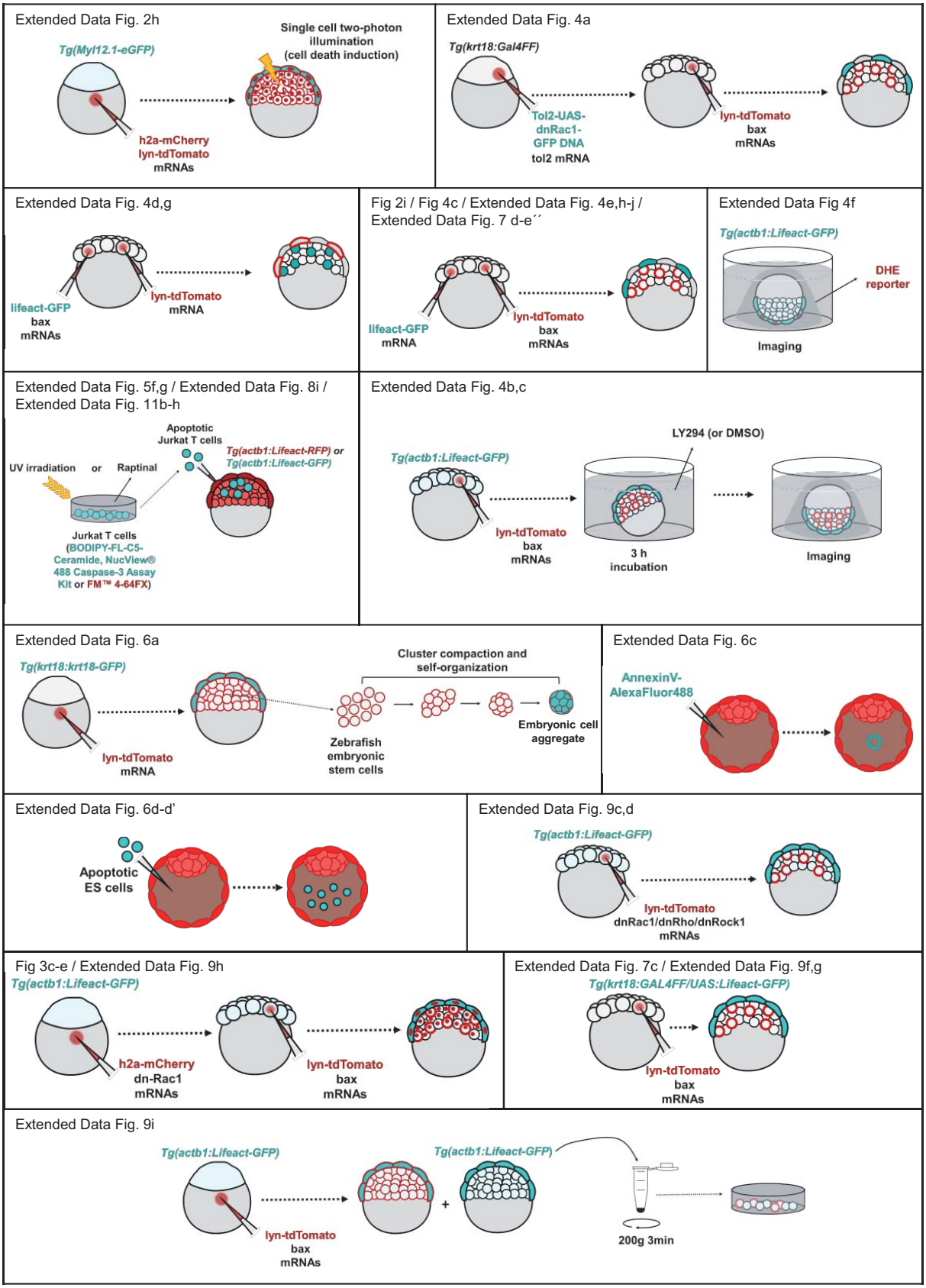

Extended data Table. Part 2. Schemes of the experiments performed detailing the staining and the corresponding figure panel.

SUPPLEMENTARY TABLE LEGEND

Supplementary Table. Differential gene expression for zebrafish EVL vs progenitor cells and mouse trophoblast vs inner cell mass cells. GO analysis for both species are also shown. Previous data from human GO analysis are also included.

Methods

Zebrafish lines and maintenance

AB wild-type zebrafish and the following transgenic lines were used: Tg(actb1:Lifeact-GFP)[3], Tg(actb1:Lifeact-RFP)[3], Tg(β-actin:myl12.1-EGFP)[4], Tg(krt18:Gal4FF)[5], Tg(krt18:krt18-GFP)[6]. Fish were maintained and bred according to the standard procedures at the aquatic facility of the Parc de Recerca Biomèdica de Barcelona (PRBB). Embryos were kept in E3 medium at 25°C–31°C prior to experiments and staged based on morphological criteria[7] and hours post fertilization (hpf). All protocols used have been approved by the Institutional Animal Care and Use Ethic Committee (PRBB–IACUEC) and were implemented according to national and European regulations. Experiments were carried out in accordance with the principles of the 3Rs.

To generate the Tg(Krt18:Gal4FF/UAS:Lifeact-GFP) line, the Tg(krt18:Gal4FF) line was injected at 1 cell stage with 25 pg of pT2AUAS:Lifeact-EGFP plasmid DNA[8] together with 25 pg of tol2 transposase mRNA, and founder fish were selected.

Subcellular staining

The following mRNAs encoding fusion proteins were synthetized from pCS2 plasmids using the SP6 mMessenger mMachine kit (Ambion) and injected at different stages: H2A-mCherry (100 pg, nuclear staining), Lyn-TdTomato and Lyn-GFP (50 pg, plasma membrane staining), Lifeact-GFP (50 pg, F-actin) and Itga5-GFP (100 pg, phagosomes). BODIPY-FL-C5-Ceramide (ThermoFisher) was used to stain cell membranes. To perform mosaic expression of Lifeact-EGFP specifically in EVL cells, the Tg(krt18:Gal4FF) line was injected with 25 pg of plasmid DNA of pT2AUAS:Lifeact-GFP (9), together with 25 pg of tol2 transposase mRNA at 1 cell stage. For Dihydroethidium (ThermoFisher Scientific) staining, 4 hpf embryos were incubated 1h with 10μm of the drug and then mounted for live imaging.

Apoptotic induction and apoptotic cell staining

To induce apoptosis, 2 pg zbax mRNA[9] (Bax^+ cells) was injected (together with lyn-TdTomato or h2a-mCherry mRNA) at 16-32 cell stage to generate mosaic embryos bearing apoptotic cells from 4 hpf, when embryos were mounted for live imaging or left to develop in E3 medium to measure survival rates. Alternatively, mosaic embryos for Caspase8-ER^{T2} fusion mRNA[10] (1 pg) were generated and treated at 4 hpf with 5 μM 4-hydroxy-tamoxifen for 1 h in solution and 2 h in the mounting agarose used for live imaging. UV irradiation with 200 mJ/cm^2 (isolated zebrafish deep cells) or 25 mJ/cm^2 (Jurkat T cells) was performed using an ultraviolet crosslinker (CL1000, UVP). Mosaic mutant Topo-II overexpression was performed injecting 100 pg mRNA for $Top2^{Y782F}$ [11] at 16-32 cell stage. For Raptinal treatments, embryos were incubated with 10 μM of the drug for 1 h in solution and 2 h in the agarose used for live imaging. To induce apoptosis in single cells with a two-photon laser, agarose mounted embryos expressing Myosin II-EGFP, Lyn-TdTomato and H2A-mCherry were mounted and imaged using a 20x glycerol immersion objective on a Leica SP5 microscope. A region of interest of about 20 μm depth from the epithelial surface with healthy stained cells was selected, and a two-photon laser beam (775 nm) was applied for 25 s on an area similar to the size of one nucleus with a digital zoom of 64x. After the illumination pulse, time-lapse imaging confirmed bleaching of the nuclear signal only in the illuminated cell, while the signal of Myosin II-EGFP remained unaltered. This induced specific morphological changes associated to apoptotic death, the appearance of a characteristic intracellular Myosin II pattern identical to Bax^+ apoptotic cells, and later epithelial phagocytic uptake of illuminated cells.

To detect apoptotic cells, 100 pg of SecA5-YFP[12] or Flip-Casp3-GFP[13] mRNA were injected at 1 cell stage. Alternatively, cells were stained *in vitro* with the NucView® 488 Caspase-3 Assay Kit for Live Cells (Biotium) or AnnexinV-Alexa Fluor™ 488 (Invitrogen), or *in vivo* with AnnexinV-AlexaFluor™ 488 by injection of about 1 nl into embryos at 4 hpf. To block phagocytosis or motility of apoptotic cells, 10 nl of AnnexinV were delivered inside the blastula cap at 4 hpf.

Expression of dominant negative proteins

Expression of dominant negative (dn) proteins was performed by injection of 20 pg dnRac1N17[14] or 40 pg dnRhoAN19[14] and dnRock1 mRNAs either at 1 cell stage (to obtain global expression) or at 16-32 cells stage (for generating mosaic embryos). In some experiments, 100 pg of H2A-mCherry mRNA was co-injected to identify cells expressing dn proteins. dnRac1 was further expressed specifically in EVL cells by injecting 25 pg of pDCG-K-GFP-UAS-RacDN plasmid DNA[15] together with 25 pg of tol2 transposase mRNA in the Tg(krt18:Gal4FF) line.

Pharmacological interference treatments
Dechorionated embryos were incubated with LY294 50 μM (Sigma) in Danieu´s solution for 3 h and then mounted for *in vivo* imaging to analyze phagocytic uptake. For dynamic analysis of apoptotic motility, embryos were pre-incubated with 50 μM SMIFH2 (Sigma) or 100 μM CK-666 (Tocris Bioscience) or DMSO (control) for 1 h in Danieau´s solution, mounted in the presence of the corresponding drugs and imaged for additional 2 h. For comparison of phagocytosis and apoptotic motility, both parameters were quantified from the time-lapse imaging performed.

Consecutive double mosaic mRNA injections in zebrafish embryos
To obtain two different populations of cells, consecutive injections were performed in the same embryo. An injection at 1 cell stage was performed to express proteins (for global staining, interference, or identification of the injected cells) in the whole embryo, followed by an injection at 16-32 cell stage to generate a population of apoptotic cells. In some cases, the injections were performed both at 16-32 cell stage in different cells, creating a double mosaic embryo with two subpopulations. In these cases, screening for the spatial proximity of the two populations was essential in order to image both populations simultaneously. In experiments based on double mosaic embryos injection for expression of dnRac1 mRNA in some cells (together with h2a-mCherry) and bax mRNA in other cells (together with lyn-TdTomato mRNA), control embryos were injected with the H2a-mCherry mRNA only in the first population. Phagocytic ability of H2a-mCherry expressing cells both in control and dnRac1 embryos was quantified. Embryos with similar levels of apoptotic cells in each condition were selected for the analysis.

Progenitor cell transplantation
For cell transplantation, apoptotic cells obtained from 4 hpf mosaic Bax-expressing Tg(actb1:Lifeact-GFP) donor embryos were identified by the co-expression of Lyn-TdTomato and increased Lifeact-GFP signal characteristic of apoptotic cells, and 15-30 cells were transplanted to a localized region close to the EVL of un-injected 4 hpf acceptor embryos of the same line using a Celltram vario device (Eppendorf).

Apoptotic surrogate targets
To generate lipid-coated apoptotic surrogate targets, 9-13 μm glass spheres (Sigma) were mixed with 80 mol% POPC1 palmitoyl-2-oleoyl-sn-glycero-3-phospholcoline (PC), 19 mol% L-α-phosphatidylserine (PS, Avanti Polar Lipids), and 1 mol% Texas Red™ 1,2-Dihexadecanoyl-sn-Glycero-3-Phosphoethanolamine (ThermoFisher Scientific) dissolved in chloroform, dried under N_2 flow and vacuum was applied for 2 h. The mix was resuspended in DMEM buffer by 5 cycles of vortexing for 30 s. A lipid mix without PS was also generated as described above, except that PS was omitted and 99 mol% PC was used. For analyzing phagocytosis and motility, 2 nl of the mix were transferred to the blastula cap of 4 hpf Tg(actb1:Lifeact-GFP) or Tg(Krt18:Gal4FF/UAS:Lifeact:EGFP) embryos using a microinjector (most of the targets transplanted were lipid aggregates, as the coated beads aggregate in the needle) and live imaging was performed. For embryo survival experiments, about 10 nl of the mix was injected in 4 hpf embryos and embryo survival was analyzed at 8 and 24 hpf. For blastocyst experiments, 5-10 lipid-coated glass beads (in this experiment the injection device allowed for transference of the coated glass beads) suspended in M2 medium were injected into the blastocyst cavity of 3.5 dpc embryos using an inverted Olympus xi71 microscope and a Cell Tram Oil Narishige microinjector.

Human Jurkat T cells culture and transplantation
Human acute leukemic Jurkat T-cells (clone E6-1, American Type Culture Collection, ATCC, Bethesa, MD, USA) were grown in RPMI 1640 medium supplemented with 10% FCS, 100 U/ml penicillin and 100 mg/ml streptomycin, 110 mg/L sodium pyruvate and 2 mM L-glutamine. Cells were maintained in a standard culture incubator with humidified air containing 5% CO2 at 37ºC. 5h after UV irradiation, the cells were stained with BODIPY-FL-C5-Ceramide (a subset were stained with AnnexinV-Alexafluor488 to evaluate apoptosis) or NucView® 488 Caspase-3 Assay Kit for live cells, injected in 4 hpf Tg(actb1:Lifeact-RFP) embryos and live imaged. For assays of uptake saturation, cells were treated with 10 μM Raptinal for 4 h, washed in DMEM medium (DMEM/F-12 with L-Glutamine and Hepes, Sigma), membrane stained with 5 μg/ml FM™ 4-64FX (ThermoFisher) for 5 min, transplanted into Tg(actb1:Lifeact-GFP) embryos and live imaged. The measured average size of phagosomes formed after epithelial uptake of apoptotic zebrafish or Jurkat T cells was not significantly different (262+/-25 μm^3 (716 phagosomes) for zebrafish cells and 310+/-24 μm^3 (941 phagosomes) for Jurkat T cells).

***In vitro* heterotypic culture**
Cultures of zebrafish progenitor cells *in vitro* were prepared at 4 hpf by vortexing manually dechorionated embryos, centrifugation, collection of the pellet in DMEM medium (DMEM/F-12 with L-Glutamine and Hepes, Sigma), and plating of the cells on a MatTek dish for live imaging. Cells obtained from Tg(actb1:Lifeact-GFP) embryos injected

with 5 pg of bax and 50 pg of lyn-TdTomato mRNA and uninjected control cells were mixed in a proportion of 1:2 to prepare the cell suspension.

Generation of self-organizing embryonic cell aggregates

10 embryos obtained from the Tg(krt18:krt18-GFP) line co-expressing Lyn-TdTomato were manually dechorionated at 6 hpf, vortexed in 1.5ml eppendorf 3x5 s, centrifuged at 200 g for 3 min and the pellet was resuspended in 20 µl of DMEM supplemented with 0.5% FBS (Gibco). Incubation for 20 min created small clusters, which were plated on MatTek dishes containing the same medium for 4 h.

Mouse experiments

The B6CBAF1 strain was used for injection of surrogate apoptotic targets or R1H2B–mCherry/GFP–GPI mES cells[17]. The B6.Cg-Tg(CAG-DsRed*MST)1Nagy/J[16] strain was used for time lapse imaging of endogenous phagocytic events and E14Tg2a ES cell injection. Mouse lines were maintained and bred according to the standard procedures at the rodent facility of Parc de Recerca Biomèdica de Barcelona (PRBB). All experiments conform to the guidelines from the European Community Directive and Spanish legislation for the experimental use of animals. Embryos were isolated from superovulated females mated with male mice. Female superovulation was induced by intraperitoneal injection of 5 international units (IU) pregnant mare's serum gonadotropin (PMSG, Biopyc, Foligon), followed by intraperitoneal injection of 5 IU human chorionic gonadotropin (hCG, Farma Higiene, Chorulon) 47 hours later. Embryos were collected in M2 (Sigma, M1167) at 0.5 dpc (days post coitum) or 2.5 dpc and cultured in 10 µL droplets of KSOM (Millipore, MR 106-D) covered with mineral oil (Sigma, M8410) at 37°C, 5% CO_2. ES cells (9-11 cells) and surrogate apoptotic targets were injected into the blastocyst cavity of 3.5 dpc embryos using an inverted Olympus xi71 microscope and a Cell Tram Oil Narishige microinjector. An Eppendorf FemtoJet microinjector was used to inject AnnexinV-AlexaFluor488. For live imaging, embryos were kept in M2 medium and imaged with a 20x (0.7 NA) glycerol-immersion objective on a Leica TCS SP5 confocal microscope equipped with an incubation chamber to keep the samples at 37°C and 5% CO2. Laser excitation of 488 nm and/or 543 nm at minimal power and HyD detectors were used.

Mouse ES cells culture

Mouse embryonic stem cells (E14Tg2a or R1H2B–mCherry/GFP–GPI[17]) were maintained in the following medium: KnockOut™ DMEM supplemented with 10% ES qualified Fetal Bovine Serum, 1 x non-essential Amino Acids Solutions, 1 x Glutamax, 50 U/mL penicillin and 50 µg/mL streptomycin, 1 x Sodium Pyruvate, 50 µM 2-mercaptoethanol, and 1000 U/mL leukemia inhibitory factor (all Life Technologies). Tissue culture-treaded dishes (Falcon) were coated with 0.1% gelatin (Sigma) for 30 min at 37°C before seeding cells. Medium was changed every 24 h and cells were passaged every other day using 0.05 % Trypsin-EDTA (Life technologies) at ratios of 1/4–1/7. Cells were grown at 37 °C in an incubator with 5% CO2. 2 days after plating, floating cells were collected (a subset stained with AnnexinV-AlexaFluor488 to evaluate apoptosis), stained with BODIPY-FL-C5-Ceramide (E14Tg2a cells) and injected in the blastocyst cavity.

RNA-seq and analysis

Cells were dissociated from Tg(krt18:krt18-GFP) embryos and $1x10^4$ GFP^+ cells were sorted in a BD Influx cell sorter (Becton Dickinson). RNA was prepared using the RNeasy Micro Kit (Qiagen) and Illumina libraries were prepared using the SMARTseq2 protocol and sequenced on a HiSeq2500 v4 to produce 50-nt single end reads. Raw Zebrafish RNA-Seq reads were processed using Nextflow: nf-core pipeline[18], using TrimGalore for adaptor and quality triming (https://github.com/FelixKrueger/TrimGalore), Star v.2.6.1d[19] to map the reads to the genome and featureCounts[20] to summarize read counts per gene. Mouse RNA-Seq reads[21] were processed using vast-tools[22] to gain raw read counts. Differential genes were calculated using DESeq2[23] using default settings, comparing GFP^+ to GFP^- cells (Zebrafish; 3 replicates), or ICM to TE (mouse). Mouse trophectoderm and ICM had to be determined from blastocyst labelled cells from[21] and split into their lineage-cell type by clustering by lineage specific markers based on previous lineage definitions[24]. Gene ontology was performed using the DAVID web knowledgebase v6.8[25] using a background of all genes expressed above a base mean of 3. Full differential expression results and gene ontology are found in Extended data Table 1.

Live imaging of zebrafish embryos

Embryos were maintained in E3 medium (5 mM NaCl, 0.17 mM KCl, 0.33 mM $CaCl_2$, 0.33 mM $MgSO_4$) until they were dechorionated and mounted in 1% low-melting point agarose in Danieau´s solution (58 mM NaCl, 0.7 mM KCl, 0.4 mM $MgSO_4$, 0.6 mM $Ca(NO_3)_2$, 5 mM HEPES) over 35 mm glass bottom Petri dishes and imaged with a 20x (0.8

NA) glycerol-immersion objective at 28ºC on Leica TCS SP5 or SP8 confocal microscopes. Laser excitation of 488 nm and 543/561 nm and HyD detectors were used. Z-stacks of 0.5-2 µm spacing between z-slices were acquired with a temporal resolution of 1 s-20 min depending on the experiment.

Image analysis

Raw data were analyzed and quantified using FIJI software [26]. Images were processed for figure preparation by applying Gaussian blur filter or despeckle function. In some cases, z-projections were shown as indicated. In Figures 1f, 2i, 4c and Extended Data Figure 3f regions of the image were cropped to improve visualization of a given structure. Quantification of phagocytic activity was done using the Cell Counter plugin from z-stacks. To measure the volume of the embryo present in the field of view, the area of the embryo in each plane was added and multiplied by the distance between planes. When measuring the initial number of apoptotic cells in embryos injected with 2 pg of bax mRNA, we estimated that 2/3 of the identified particles correspond to intact cells and the other 1/3 to cell fragments. Phagosomes were identified by the red signal originating from the Lyn-TdTomato marker expressed in apoptotic cells. To unequivocally count phagosomes, particles smaller than 3 µm were discarded from the analysis. Apoptotic fragments not ingested by the EVL cells were identified by the red signal, an increased Lifeact-GFP signal, and by characteristic morphology. To quantify the dynamics of fluorescence signals in phagosomes, individual phagosomes were tracked over time and the mean signal (GFP), or the coefficient of variance (standard deviation/mean) were estimated. The volume uptaken by each EVL cell was calculated measuring the diameter of each phagosome assuming a spherical geometry. Once the volume uptaken by all EVL cells was calculated at each time frame, the 20 cells with higher uptake volume were selected and used for the saturation analysis.

Apoptotic motility was quantified using the MTrackJ plugin[27], from which instantaneous speed, track length, x-y-z positions, and visualization were obtained. The mean speed for each track is an average of the instantaneous speed obtained for each time frame. Fast phases of apoptotic motility were defined as periods of 4-10 frames in which at least 2/3 of the frames show an instantaneous speed >10 µm/min. Maximum speed values correspond to the maximal instantaneous speed achieved by each apoptotic cell. To select the cells to be tracked, fast moving apoptotic cells were identified and then manually tracked in 3D. Representations of the apoptotic paths were done in 2D using only the x-y coordinates (z-coordinate provides a minor contribution to the whole movement). To construct the kymographs, a region from a time-lapse of one z-plane was resliced, following the signal in the region selected over time. Quantification of intensity of the fluorescent signals were done on raw images using the Plot Profile function. To quantify the frequency of phagocytic cup formation, successful phagocytic events were considered. To quantify the frequency of arm formation, rear actin accumulation associated to fast motile apoptotic cells lasting for a minimum period of 1.5 min was identified. To determine the association of apoptotic motility and rear external actin in EVL-specific stained embryos, the presence of actin in contact with the apoptotic cell was analyzed in previously identified motile cells. To determine the number of EVL cells faced by apoptotic cells, we tracked apoptotic cells before uptake counting the contact with each individual epithelial cell, neglecting multiple encounters with the same epithelial cells. For cells not uptaken (live cells or apoptotic cells in CK-666 and dnRac1 embryos), tracks with the same time of travel than uptaken ones were used.

Curvature analysis of apoptotic target cells during phagocytic uptake

Raw images of apoptotic Bax^+ cells during epithelial phagocytosis were analyzed using custom written scripts in Matlab (Mathworks 2017b). First, a 2D cell outline was manually defined and interpolated by a spline function with zero tension. From the obtained 2D curve, the curvature vector was determined by adapting an open-source Matlab code[28]. Normal directions of curvature vectors (pointing inside versus outside) indicate positive versus negative curvature values of the surface and were used to derive scalar local curvature values which were further normalized to represent color-coded bending values along the apoptotic fragment cross-section.

Analysis of actin density versus movement directionality

Apoptotic targets during active pushing phases were analyzed using two-color fluorescence raw images to derive the movement directionality of apoptotic fragments and to measure accompanying actin densities generated by pushing epithelial arms along the apoptotic target cross-sectional perimeter. At a specific time point *t*, the change in target movement direction between $\left(\vec{x}(t+1)-\vec{x}(t)\right)$ in relation to the previous direction $\left(\vec{x}(t)-\vec{x}(t-1)\right)$ was measured and plotted in an angular histogram (t_{lag} =1 min). In addition, the actin density of epithelial arm protrusions in contact with apoptotic targets was extracted at a time point *t* by manually outlining the cross-sectional area of the apoptotic target shape. Fluorescence intensity values were averaged along the line profile (line of 5 Pixel width) at the target surface. Shape outlines were normalized to the total cross-sectional perimeter of apoptotic cells and intensity values were plotted as color-coded values along a normalized unit circle oriented along the target direction at *t*.

Single cell tracking analysis

Raw data were tracked manually as described above and further analyzed using custom-written scripts in Matlab (Mathworks 2017b). To compare representative x-y trajectories, arbitrarily selected tracks were centered to the origin and cut at the indicated maximum track length. Rose plot diagrams were calculated from tracks at time intervals (t_{lag} = 3 frames of 38-50 sec) to generate a histogram of angle distributions between consecutive steps in the trajectories. Mean Square Displacement (MSD) analysis was performed on manually tracked apoptotic and live cell data. The MSD curves were obtained as:

$$MSD(tlag) = \langle(\vec{x}\,(t + tlag) - \vec{x}\,(t))^2\rangle$$

with errorbars calculated as previously described[29]. The MSD versus time data for live cell trajectories were fitted to a diffusion model with flow:

$$MSD(tlag) = \alpha \cdot v^2 t^2 + (1 - \alpha) \cdot 4 \cdot D \cdot t.$$

MSD versus time data of apoptotic cells were fitted to a persistent random walk model:

$$MSD(tlag) = 4 \cdot D \cdot \left(t - P_t \left(1 - e^{-\frac{t}{P_t}}\right)\right).$$

Statistical tests

Statistical significance tests were performed with either (1) the two-sample t-test when the data followed a normal distribution or (2) a non- parametric KS (Matlab) otherwise. Mean and standard errors were calculated using Excel (Microsoft). Unpaired Student's t-test and p values were calculated using GraphPad.

Monte Carlo simulations of the clearance model

Extended Data Fig. 10a shows a model representation of the dynamic clearance process given a number of apoptotic cells N_{target} underneath a one-dimensional epithelial layer. A number of epithelial cells (N_{EVL}) of size L=20 μm are aligned next to each other, yielding a total epithelial layer $L*N_{EVL}$. EVL cells can either uptake apoptotic fragments with probability p_{up} or actively push fragments with probability p_v in the lateral directions, leading to target dispersal under the epithelial layer. Pushing periods (with velocity v) exclude uptake of fragments, resulting in a conditional uptake probability of $(1-p_v)p_{up}$. Each EVL cell is assumed to have a limited uptake capacity of apoptotic target particles defined by N_{max}, providing an upper boundary to the total volume an individual EVL cell can ingest. Initial conditions of the simulations were set via positioning N_{target} cells at the center of the epithelial layer. The time during target pushing t_{off} defines the simulation time steps during which the number of free targets N_{target}, which have not been uptaken yet, can either be actively pushed in lateral directions (p_{right}=p_{left}=0.5) or uptaken with probability $(1-p_v)p_{up}$. The pushing events with velocity v generate a persistence length of target movement given by $l_p=v\ t_{off}$. The simulation process is repeated k times until all apoptotic fragments are uptaken. The spatial domain length of the epithelial layer is set to allow for full target clearance $N_{EVL}>>N_{target}/N_{max}$.

Supplementary notes

We briefly describe here the derivation of the formula to calculate the apoptotic clearance time in the presence of phagocytic arm pushing speed, v. The model assumes a cluster of N_{target} apoptotic cells ("targets") at an initial time $t=0$, located at a position $x=0$ directly underneath a one-dimensional layer of epithelial cells (see sketch in Extended Data Fig. 10a). We assume that the targets can be treated as point particles, with negligible spatial extent. Each epithelial cell, of width L, can engulf N_{max} targets. The clearance time, t_{clear}, is largely independent of the phagocytic uptake rate p_{up}, suggesting that clearance is diffusion-limited. Following the experimental results, we modeled individual pushing events as a directional motion with a speed $+/-v$ during time t_{off}. The probability for pushing is described by p_v leading to particle displacements $l_p=v\ t_{off}$ during the time $(1/p_v)t_{off}$. On times large compared with t_{off} this results in a random walk with an effective diffusion constant $D_{\mathrm{eff}} = 1/2 \cdot p_v v^2 t_{\mathrm{off}}$. We assume that at a time $t > 0$ there is a boundary position $s(t) \sim \sqrt{D_{\mathrm{eff}}\, t}$ such that epithelial cells in the region $-s(t) < x < s(t)$ have each engulfed N_{max} targets, while those lying outside this region are empty of targets. As a result, the clearance time can be defined as the moment when $2\ N_{\mathrm{max}}\ s(t_{\mathrm{clear}}) = N_{\mathrm{target}} \cdot L$, leading to

$$t_{\mathrm{clear}} = \left(\frac{N_{\mathrm{target}}}{N_{\mathrm{max}}}\right)^2 \frac{L^2}{2\ p_v\ v^2 t_{\mathrm{off}}}.$$

This formula predicts that the clearance time decreases with the square of the arm pushing speed v (see Fig. 4i and Extended Data Fig. 10b) and with the square of the loading capacity, N_{max}, in agreement with simulations (see Extended Data Fig. 10c).

Captions for Videos 1 to 14

Supplementary Video 1. Single cell dynamics of endogenous apoptotic events and epithelial uptake. The enveloping epithelial layer (EVL) uptakes apoptotic cells as identified by morphological features (I, yellow lines indicate apoptotic cell fragment paths), AnnexinV-YFP (II, cyan) binding, or activated Capase-3 (III, cyan; yellow and white lines indicate apoptotic and live cell paths, respectively). Myosin II-EGFP (I, cyan), plasma membrane (PM, Lyn-tdTomato, red, I,II,III) and nucleus (H2a-mCherry, red, I) are shown. White and green arrowheads indicate apoptotic fragments before and after epithelial uptake (note that fragments from a single apoptotic cell are uptaken by different epithelial cells).

Supplementary Video 2. Errors in cell division (I), associated to cell death (II), and to cell death and epithelial uptake (III). Lifeact-GFP (I and II, cyan), Myosin II-EGFP (III, cyan), plasma membrane (Lyn-tdTomato, red, I,II,III) and nucleus (H2a-mCherry, red, I, II, III) are shown.

Supplementary Video 3. EVL clearance dynamics of Bax^+ apoptotic cells (I, co-expressing the PM marker Lyn-tdTomato, red). Embryo expressing Lifeact-GFP (cyan). (II) Dynamics of Caspase-3 reporter activation (cyan) in Bax^+ cells during nuclear (H2a-mCherry, red) fragmentation.

Supplementary Video 4. Epithelial clearance under stress conditions. Mosaic mutant Topo-II expression (I), whole embryo Raptinal treatment (II), single cell 2-photon induced programmed cell death (III) and mosaic Caspase-8 activation (IV). PM (Lyn-tdTomato, red) or nucleus (H2a-mCherry, red) in apoptotic cells (I, IV) or in the whole embryo (II, III), F-actin (Lifeact-GFP, cyan, I, IV) and Myosin II-EGFP (cyan, II and III) are shown.

Supplementary Video 5. Single cell visualization of epithelial phagocytosis of Bax^+ cells. (I) Two examples of z-projections of phagocytic cups showing an actin ring, and single slices with sections parallel and transverse to the epithelial surface showing the dynamics of phagocytic pseudopods. (II) Phagocytic cup formed from epithelial ruffles. F-actin (Lifeact-GFP, cyan) and PM of apoptotic cells (Lyn-tdTomato, red) are shown. (III) Degradation of the apoptotic debris after uptake. Double mosaic showing F-actin (Lifeact-GFP, cyan) in an epithelial cell and PM of apoptotic cells (Lyn-tdTomato, red) are shown.

Supplementary Video 6. Epithelial clearance of PS^+ surrogate apoptotic targets. Global (I, parallel and transverse sections) or high magnification epithelial-specific staining (II) for F-actin (Lifeact-GFP, cyan) are shown. PM of Bax^+ cells is shown (Lyn-tdTomato, red).

Supplementary Video 7. Mouse trophoblast uptakes apoptotic particles. Uptake of an apoptotic cells released from the inner cell mass (I), uptake of an *in vivo* stained apoptotic cell in the cavity by AnnexinV-AlexaFluor488 injection (cyan, II), and uptake detail of an apoptotic ES cell injected in the cavity (III). Blastocysts express DsRed (red), and ES cells are stained with Bodipy-FL-C5 ceramide (cyan).

Supplementary Video 8. *In vivo* apoptotic motility in association with actin arms. Whole embryo (I) or detailed view (II) of Bax^+ cells (co-expressing Lyn-tdTomato, red) moving fast and non-directionally along the embryo in association with external F-actin (Lifeact-GFP, cyan). An embryo with mosaic PM (Lyn-tdTomato) staining of motile live cells with slow and directional movement in comparison to apoptotic cells is shown on the right (I). Tracks are depicted by yellow (apoptotic cells) or white (live cells) lines.

Supplementary Video 9. High speed imaging of *in vivo* actin filament dynamics (Lifeact-GFP, cyan) in association with the external rear surface of single Bax^+ apoptotic cells (PM, Lyn-tdTomato, red).

Supplementary Video 10. Dynamics of epithelial arms and ruffles. (I) Single cell epithelial arm visualization (Lifeact-GFP, cyan) in association with a Bax^+ apoptotic cell (PM, Lyn-tdTomato, red). (II) Ruffles in an embryo expressing Lifeact-GFP (cyan) and showing Bax^+ apoptotic cells (PM, Lyn-tdTomato, red).

Supplementary Video 11. Arm-mediated motility of endogenous apoptotic cells. (I) Epithelial actin contacting a dead cell and polarizing to the cell rear to initiate motility and (II) Phagocytic uptake and epithelial arms associated to motility of an endogenous cell dying after an error in mitosis. Lifeact-GFP (cyan), PM (Lyn-tdTomato, red), and H2a-mCherry (nucleus, red) are shown.

Supplementary Video 12. (I) Epithelial arms (Lifeact-RFP, red) formed in contact with apoptotic Jurkat T cells (Bodipy-FL-C5-Ceramide, cyan). (II) Apoptotic motility after transplantation of few UV-irradiated cells (Lifeact-GFP, cyan; PM, Lyn-tdTomato, red). (III) *In vivo* single cell Myosin II dynamics (Myosin II-EGFP, cyan) in a single Bax^+ apoptotic cell (PM, Lyn-tdTomato, red). (IV) Epithelial-specific actin (cyan) associates with motile Bax^+ apoptotic cells (PM, Lyn-tdTomato, red). Embryos are Tg(Krt18:Gal4FF/UAS:Lifeact-GFP) .

Supplementary Video 13. (I) Loss of epithelial arm protrusions and apoptotic cell motility (Bax and Lyn-tdTomato, red plasma membrane) in dnRac1-expressing (H2a-mCherry, red nucleus) embryos. F-actin is shown (Lifeact-GFP, cyan). (II) Epithelial arms (Lifeact-GFP, cyan) push PS^+ surrogate targets (Texas Red-DHPE, red). (III) CK-666-mediated Arp2/3 inhibition blocks apoptotic motility, arm formation, and phagocytic uptake. (IV) SMIFH2-mediated Formin inhibition blocks phagocytic uptake but does not affect epithelial arm formation and apoptotic motility. In III and IV embryos express Lifeact-GFP (cyan) and apoptotic cells express Bax and Lyn-tdTomato (red).

Supplementary Video 14. (I) Consecutive pushing of an apoptotic cell by arms coming from different epithelial cells. F-actin (cyan) and a Bax^+ cell (co-expressing Lyn-tdTomato, red) are shown. (II) Tracking of Bax^+ apoptotic cells (co-expressing Lyn-tdTomato, yellow dots) after transplantation into a localized region underneath the EVL of an acceptor Tg(actb1:Lifeact-GFP) embryo. A pool of epithelial cells initially in close proximity to the transplanted cells are depicted in blue, and cells for the expanded epithelial area after apoptotic spreading are shown in magenta.

References

1 Shinoda, H., Shannon, M. & Nagai, T. Fluorescent Proteins for Investigating Biological Events in Acidic Environments. *Int J Mol Sci* 19, doi:10.3390/ijms19061548 (2018).

2 Delamarre, L., Pack, M., Chang, H., Mellman, I. & Trombetta, E. S. Differential lysosomal proteolysis in antigen-presenting cells determines antigen fate. *Science* 307, 1630-1634, doi:10.1126/science.1108003 (2005).

3 Behrndt, M. *et al.* Forces driving epithelial spreading in zebrafish gastrulation. *Science* 338, 257-260, doi:10.1126/science.1224143 (2012).

4 Maitre, J. L. *et al.* Adhesion functions in cell sorting by mechanically coupling the cortices of adhering cells. *Science* 338, 253-256, doi:10.1126/science.1225399 (2012).

5 Kajita, M. *et al.* Interaction with surrounding normal epithelial cells influences signalling pathways and behaviour of Src-transformed cells. *J Cell Sci* 123, 171-180, doi:10.1242/jcs.057976 (2010).

6 Xia, P., Gutl, D., Zheden, V. & Heisenberg, C. P. Lateral Inhibition in Cell Specification Mediated by Mechanical Signals Modulating TAZ Activity. *Cell* 176, 1379-1392 e1314, doi:10.1016/j.cell.2019.01.019 (2019).

7 Kimmel, C. B., Ballard, W. W., Kimmel, S. R., Ullmann, B. & Schilling, T. F. Stages of embryonic development of the zebrafish. *Dev Dyn* 203, 253-310, doi:10.1002/aja.1002030302 (1995).

8 Helker, C. S. *et al.* The zebrafish common cardinal veins develop by a novel mechanism: lumen ensheathment. *Development* 140, 2776-2786, doi:10.1242/dev.091876 (2013).

9 Popgeorgiev, N. *et al.* The apoptotic regulator Nrz controls cytoskeletal dynamics via the regulation of Ca2+ trafficking in the zebrafish blastula. *Dev Cell* 20, 663-676, doi:10.1016/j.devcel.2011.03.016 (2011).

10 Weber, T. *et al.* Caspase-mediated apoptosis induction in zebrafish cerebellar Purkinje neurons. *Development* 143, 4279-4287, doi:10.1242/dev.122721 (2016).

11 Furniss, K. L. *et al.* Direct monitoring of the strand passage reaction of DNA topoisomerase II triggers checkpoint activation. *PLoS Genet* 9, e1003832, doi:10.1371/journal.pgen.1003832 (2013).

12 van Ham, T. J., Kokel, D. & Peterson, R. T. Apoptotic cells are cleared by directional migration and elmo1-dependent macrophage engulfment. *Curr Biol* 22, 830-836, doi:10.1016/j.cub.2012.03.027 (2012).

13 Zhang, Q. *et al.* Designing a Green Fluorogenic Protease Reporter by Flipping a Beta Strand of GFP for Imaging Apoptosis in Animals. *J Am Chem Soc* 141, 4526-4530, doi:10.1021/jacs.8b13042 (2019).

14 Tahinci, E. & Symes, K. Distinct functions of Rho and Rac are required for convergent extension during Xenopus gastrulation. *Dev Biol* 259, 318-335, doi:10.1016/s0012-1606(03)00206-9 (2003).

15 Hanovice, N. J., McMains, E. & Gross, J. M. A GAL4-inducible transgenic tool kit for the in vivo modulation of Rho GTPase activity in zebrafish. *Dev Dyn* 245, 844-853, doi:10.1002/dvdy.24412 (2016).

16 Vintersten, K. *et al.* Mouse in red: red fluorescent protein expression in mouse ES cells, embryos, and adult animals. *Genesis* 40, 241-246, doi:10.1002/gene.20095 (2004).

17 Nowotschin, S., Eakin, G. S. & Hadjantonakis, A. K. Dual transgene strategy for live visualization of chromatin and plasma membrane dynamics in murine embryonic stem cells and embryonic tissues. *Genesis* 47, 330-336, doi:10.1002/dvg.20500 (2009).

18 Ewels, P. A. nf-core: Community curated bioinformatics pipelines. *bioRxiv*, doi:doi: 10.1101/610741 (2019).

19 Dobin, A. *et al.* STAR: ultrafast universal RNA-seq aligner. *Bioinformatics* 29, 15-21, doi:10.1093/bioinformatics/bts635 (2013).

20 Liao, Y., Smyth, G. K. & Shi, W. featureCounts: an efficient general purpose program for assigning sequence reads to genomic features. *Bioinformatics* 30, 923-930, doi:10.1093/bioinformatics/btt656 (2014).

21 Deng, Q., Ramskold, D., Reinius, B. & Sandberg, R. Single-cell RNA-seq reveals dynamic, random monoallelic gene expression in mammalian cells. *Science* 343, 193-196, doi:10.1126/science.1245316 (2014).

22 Irimia, M. *et al.* A highly conserved program of neuronal microexons is misregulated in autistic brains. *Cell* 159, 1511-1523, doi:10.1016/j.cell.2014.11.035 (2014).

23 Love, M. I., Huber, W. & Anders, S. Moderated estimation of fold change and dispersion for RNA-seq data with DESeq2. *Genome Biol* 15, 550, doi:10.1186/s13059-014-0550-8 (2014).

24 Guo, G. *et al.* Resolution of cell fate decisions revealed by single-cell gene expression analysis from zygote to blastocyst. *Dev Cell* 18, 675-685, doi:10.1016/j.devcel.2010.02.012 (2010).

25 Huang DA, S. B., Lempicki RA. Systematic and integrative analysis of large gene lists using DAVID bioinformatics resources. *Nature Protocols* 4, 44-57 (2009).

26 Schindelin, J. *et al.* Fiji: an open-source platform for biological-image analysis. *Nat Methods* 9, 676-682, doi:10.1038/nmeth.2019 (2012).
27 Meijering, E., Dzyubachyk, O. & Smal, I. Methods for cell and particle tracking. *Methods Enzymol* 504, 183-200, doi:10.1016/B978-0-12-391857-4.00009-4 (2012).
28 Mjaavatten, A. Curvature of a 2D or 3D curve *(https://www.mathworks.com/matlabcentral/fileexchange/69452-curvature-of-a-2d-or-3d-curve)* (2019).
29 Qian, H., Sheetz, M. P. & Elson, E. L. Single particle tracking. Analysis of diffusion and flow in two-dimensional systems. *Biophys J* 60, 910-921, doi:10.1016/S0006-3495(91)82125-7 (1991).